NuMorph: tools for cellular phenotyping in tissue cleared whole brain images

Oleh Krupa[1,2,3], Giulia Fragola[2,4,5], Ellie Hadden-Ford[2,3], Jessica T. Mory[2,3], Tianyi Liu[2,3,6], Zachary Humphrey[2,3], Ashok Krishnamurthy[7], Mark J. Zylka[2,4], Guorong Wu[8,9], and Jason L. Stein[2,3,10,*]

1) Joint Department of Biomedical Engineering, University of North Carolina at Chapel Hill and North Carolina State University, Chapel Hill, North Carolina 27514, USA
2) UNC Neuroscience Center, University of North Carolina at Chapel Hill, Chapel Hill, NC 27599, USA
3) Department of Genetics, University of North Carolina at Chapel Hill, Chapel Hill, NC 27599, USA
4) Department of Cell Biology and Physiology, University of North Carolina at Chapel Hill, Chapel Hill, NC, 27599, USA
5) Department of Neurology, University of North Carolina at Chapel Hill, Chapel Hill, NC 27599, USA
6) Department of Biostatistics, University of North Carolina at Chapel Hill, Chapel Hill, NC 27599 USA
7) Renaissance Computing Institute, Chapel Hill, NC 27599, USA
8) Department of Psychiatry, University of North Carolina at Chapel Hill, Chapel Hill, NC 27514, USA
9) Department of Computer Science, University of North Carolina at Chapel Hill, Chapel Hill, NC 27514, USA
10) Lead Contact
Correspondence: jason_stein@med.unc.edu

Abstract

Tissue clearing methods allow every cell in the mouse brain to be imaged without physical sectioning. However, the computational tools currently available for cell quantification in cleared tissue images have been limited to counting sparse cell populations in stereotypical mice. Here we introduce NuMorph, a group of image analysis tools to quantify all nuclei and nuclear markers within the mouse cortex after tissue clearing and imaging by a conventional light-sheet microscope. We applied NuMorph to investigate a *Topoisomerase 1* (*Top1*) conditional knockout mouse model with severe brain structure deficits and identified differential effects of *Top1* deletion on cortical cell-types and structures that were associated with spatial patterns of long gene expression. These tools are applicable for the study of 3D cellular level structural deficits in brains from other animal models of neuropsychiatric disorders.

Introduction

The mammalian cortex is composed of a diverse assembly of cell-types organized into complex networks, which function together to enable complex behaviors (Harris et al., 2019; Tasic et al., 2018; Zeisel et al., 2015). Disruption of cortical cytoarchitecture, either by genetic or environmental perturbation, can lead to altered brain function and create risk for neuropsychiatric disorders (Shin Yim et al., 2017; Stoner et al., 2014). A common approach for

42   studying the mechanisms by which genetic variation increases risk for neuropsychiatric
43   disorders is through the use of genetically modified animal models in a WT/KO experimental
44   design. In order to observe the causal effects of disorder relevant genes on structure-function
45   relationships, genetic tools can be applied to activate or silence genes in specific cell-types
46   (Tsien et al., 1996) by imaging cellular organization through fluorescence microscopy. One
47   critical goal in such experiments is to determine if the number of cells of a given type are altered
48   by these genetic risk factors throughout different brain structures. However, a common limitation
49   in imaging experiments done at cellular resolution is that they are restricted to anatomical
50   regions of interest by physical sectioning which prevents the detection of region-specific effects.
51   This becomes a particular issue for the cortex, one of the largest structures in the brain (Wang
52   et al., 2020), where heterogeneity between cortical areas is often unmeasured by standard
53   methods.
54
55   In order to image the entire brain without physical sectioning, tissue clearing methods render
56   biological specimens transparent while preserving their 3 dimensional structure. Cleared tissues
57   can then be rapidly imaged using light-sheet microscopy as plane illumination improves
58   acquisition rates by 2-3 orders of magnitude compared to point scanning systems while also
59   limiting the effects of photobleaching (Richardson and Lichtman, 2015; Ueda et al., 2020). Great
60   strides have been made in the development of clearing protocols that are compatible with
61   immunolabeling and the design of complementary sophisticated imaging systems (Matsumoto
62   et al., 2019; Murray et al., 2015; Park et al., 2018; Susaki et al., 2020). Yet challenges still
63   remain in expanding the accessibility of these technologies to research labs for quantitative
64   analysis at cellular resolution.
65
66   For example, many of the current imaging protocols for whole brain profiling require custom light
67   sheet systems to image tissues at cellular resolution (Fei et al., 2019; Matsumoto et al., 2019;
68   Pende et al., 2018; Tomer et al., 2014; Voigt et al., 2019). These systems are therefore
69   inaccessible to those lacking the expertise or resources required to assemble the necessary
70   microscope components. Expanding tissues during the clearing process is a potential
71   workaround that can increase the effective spatial resolution allowing for interrogation of
72   subcellular structures without the need for custom imaging solutions (Chen et al., 2015; Gao et
73   al., 2019; Ku et al., 2016; Murakami et al., 2018). However, expanded tissues can fall outside of
74   the working distance of conventional microscope objectives and require prolonged imaging
75   times with significantly larger data storage resources. Therefore, computational tools designed
76   for conventional light sheet microscope users are needed to compare cell counts in a WT/KO
77   design.
78
79   With over 100 million cells in a mouse brain and image sizes of tissue cleared brain
80   approaching terabytes, advanced image analysis tools are needed to achieve accurate cell
81   quantification. Current segmentation methods for tissue cleared brain images apply a threshold
82   for nuclear staining intensity and filter objects with a predefined shape, size, and/or density
83   (Renier et al. 2016; Matsumoto et al. 2019; Fürth et al. 2018). However, variations in cell size,
84   image contrast, and labeling intensity can all lead to inaccurate counts. In addition, whole brain
85   images are typically registered to a standard reference, such as the Allen Reference Atlas

86 (ARA), to assign cell locations to their corresponding structural annotations. Thus far, image
87 registration has been performed mostly on stereotypical mice and has not been designed for
88 mouse models with significant changes in gross morphology. With these limitations, the
89 computational tools currently available have not been fully adopted for studying cellular
90 organization in mouse models.
91
92 To address these issues, we developed a group of image analysis tools called NuMorph
93 (Nuclear-Based Morphometry) (available here: https://bitbucket.org/steinlabunc/numorph/) for
94 end-to-end processing to perform cell-type quantification within the mouse cortex after tissue
95 clearing and imaging by a conventional light-sheet microscope. To demonstrate the
96 effectiveness of the tool, we applied and evaluated NuMorph to quantify structural changes in a
97 mouse model with strong differences in cortical structure, a topoisomerase I (*Top1*) conditional
98 knockout (*Top1* cKO) mouse model that exhibits clear reductions in both cortical size and
99 specific cell types (Fragola et al., 2020). Our results reveal cell-type and structure specific
100 effects caused by *Top1* deletion and demonstrate the broad applicability of our analysis tools for
101 studying severe brain structure phenotypes in combination with tissue clearing methods.

Methods
102

Animals
103

104 *Top1* conditional knockout mice (*Neurod6$^{Cre/+}$::Top1$^{fl/fl}$* , *Top1* cKO) were bred by crossing
105 *Top1$^{fl/fl}$* mice (Mabb et al., 2016) with the *Neurod6^{Cre}* mouse line (Jackson Laboratory)
106 (Goebbels et al., 2006) as described previously (Fragola et al., 2020). All animal procedures
107 were approved by the University of North Carolina at Chapel Hill Institutional Animal Care and
108 Use Committee. Mice were maintained on a 12-hr dark/light cycle and housed at temperatures
109 of 18-23°C, 40-60% humidity, and *ad libitum* food and water. Genomic DNA extracted from tail
110 or ear samples was utilized for genotyping by PCR. Primers for gene amplification are as
111 follows (listed 5'-3'): *Top1*-F: GAGTTTCAGGACAGCCAGGA, *Top1*-R:
112 GGACCGGGAAAAGTCTAAGC; Cre-F: GATGGACATGTTCAGGGATCGCC, Cre-R:
113 CTCCCATCAGTACGTGAGAT. Male P15 *Top1* cKO were used for tissue clearing experiments
114 along with WT (*Neurod6$^{+/+}$::Top1$^{fl/fl}$*) littermate controls.

Tissue Clearing & Immunolabeling
115

116 Tissue clearing was performed on 4 WT and 4 *Top1* cKO according to the iDISCO+ protocol
117 (Renier et al., 2016). Briefly, P15 mice were fixed via transcardial perfusion using 4%
118 paraformaldehyde and whole brain samples were dissected and cut along the midline. As the
119 effects of *Top1* deletion on gross structure were bilateral upon visual inspection, only the left
120 hemisphere was used in clearing experiments and analysis. Samples were then washed in
121 phosphate-buffered-saline (PBS), dehydrated in a graded series of methanol (Fisher, A412SK),
122 pretreated with 66% dichloromethane (Sigma- Aldrich, 270997)/methanol and 5% H2O2
123 (Sigma-Aldrich, H1009)/methanol, followed by rehydration, permeabilization (20% dimethyl-
124 sulfoxide, Fisher, BP2311; 1.6% Triton X100, Sigma-Aldrich, T8787; 23mg/mL Glycine, Sigma-
125 Aldrich G7126), and blocking with 6% goat serum (Abcam, ab7481). Samples were then

126   incubated with antibodies for Cux1 (Santa Cruz, sc-13024-Rb, 1:200) and Ctip2 (Abcam,
127   ab18465-Rt, 1:500) for 5 days at 37°C in PTwH buffer (PBS; 0.5% Tween-20, Fisher, BP337;
128   10mg/L Heparin, Sigma-Aldrich, H3393) . After 2 days of washing with PTwH, samples were
129   then incubated with TO-PRO-3 (Thermo Fisher, T3605, 1:300), goat anti-rat Alexa Fluor 568
130   (Thermo Fisher, A11077, 1:200), and goat anti-rabbit Alexa Fluor 790 (Thermo Fisher, A11369,
131   1:50) for an additional 5 days at 37°C. Samples were then washed for 2 days with PTwH,
132   dehydrated again using a graded methanol series, incubated in 66% dichloromethane/methanol
133   for 3 hours, followed by a 30 minute incubation in 100% dichloromethane before storing in a
134   dibenzyl ether solution (RI = 1.56, Sigma-Aldrich, 108014) at RT. Tissue clearing and antibody
135   labeling required 21 days to complete.

Light-Sheet Imaging

137   Imaging of cleared brain samples was performed using the Ultramicroscope II (LaVision Biotec)
138   equipped with MVPLAPO 2X/0.5 NA objective (Olympus), sCMOS camera (Andor), and
139   ImSpector control software. The zoom body was set to 2.5x magnification (yielding 1.21
140   µm/pixel) and a single light sheet was used with NA = 0.085 (9 µm thickness/ 4 µm z-step) as
141   this showed increased axial resolution for cell nuclei compared to using multiple light sheets.
142   Dynamic horizontal focusing using the contrast enhanced setting in ImSpector was used to
143   ensure axial resolution was maintained along the width of the image using the recommended
144   number of steps depending on the laser wavelength. In addition, images were partially cropped
145   by ~20% around the edges to a region of interest at the center (~2100x1800 pixels) to limit
146   radial aberrations at the corners of the field of view due to the camera lens tube. Samples were
147   positioned sagittally with the cortex surface facing the single illuminating light-sheet (Figure
148   S1D). This prevented excessive light scattering and shadowing from affecting the image quality
149   in the cortical regions. Individual channels were acquired for tiled positions in a row-major order
150   using 561nm (Ctip2), 647nm (ToPro), or 785nm (Cux1) laser lines. The 785nm channel was
151   imaged first for the entire hemisphere. After refocusing the objective, the 561nm/647nm
152   channels were then captured sequentially for each stack at a given tile position. Using these
153   settings, WT mouse hemispheres were acquired using a 4x4 tiling scheme with 15% overlap (5-
154   7 hours per channel) while *Top1* cKO hemispheres were acquired using a 3x3 tiling scheme (3-
155   4 hours per channel) due to their significantly reduced size.

Computing Resources

157   All data processing was performed locally on a Linux workstation running CentOS 7. The
158   workstation was equipped with an Intel Xeon E5-2690 V4 2.6GHz 14-core processor, 8 x 64GB
159   DDR4 2400 LRDIMM memory, 4 x EVGA GeForce GTX 1080 Ti 11GB GPU, and 2 x 4TB
160   Samsung EVO 860 external SSDs. Hot swap bays were used to transfer data from the imaging
161   computer to the analysis workstation.

Image Preprocessing

163   Image preprocessing consists of all the necessary steps to prepare acquired raw images for
164   image registration and cell quantification. All preprocessing steps were performed using custom
165   written MATLAB R2020a scripts included in NuMorph and are described below.

4

166 Intensity Adjustments

167 Two types of image intensity adjustments were performed on raw images prior to image
168 stitching to increase accuracy of subsequent processing. First, uneven illumination along the *y*
169 dimension (perpendicular to the light path) of each 2D image caused by the Gaussian shape of
170 the light sheet was corrected using a MATLAB implementation of BaSiC, a tool for retrospective
171 shading correction (Peng et al., 2017). We used 10% of all images, excluding tile positions
172 around the cerebellum, to estimate a flatfield image for each channel. Each image was then
173 divided by the flatfield prior to alignment and stitching to correct for uneven illumination. Second,
174 differences in intensity distributions between image tile stacks, primarily as a result of
175 photobleaching and light attenuation, were measured in the horizontal and vertical overlapping
176 regions of adjacent tiles. To ensure bright features were of equal intensity between each stack,
177 we measured the relative difference (t^{adj}) in the 95th percentile of pixel intensities in
178 overlapping regions from 5% of all images. The measured image intensity I^{meas} at tile location
179 $(x, y)$was then adjusted according to:

180
181 $$I^{adj}(x,y) \; = \; (I^{meas}(x,y) - D) * t^{adj}(x,y) + D$$
182
183 where $D$is the darkfield intensity (set as a constant value based on the 5th percentile of pixel
184 intensities in all measured regions).

185 Image Channel Alignment

186 As image channels are acquired one at a time, subtle drift in stage and sample positions during
187 imaging may result in spatial misalignment between the reference nuclei channel and the
188 remaining immunolabeled markers in a multichannel image. We tested two image registration
189 approaches to ensure robust alignment across image channels. The first approach estimates
190 2D slice translations to align the immunolabeled channel images to the nuclear channel image.
191 The axial (*z*) correspondence between the nuclei channel and every other channel within an
192 image stack of an individual tile is first estimated using phase correlation at 20 evenly spaced
193 positions within the stack. The correspondence along the axial direction with the highest image
194 similarity (based on intensity correlation) determines the relative tile *z* displacement between
195 channels (up to 50 μm in some cases). *xy* translations are then determined after multimodal
196 image registration for each slice in the tile stack using MATLAB's Image Processing toolbox.
197 Outlier translations, defined as *x* or *y* translations greater than 3 scaled median absolute
198 deviations within a local 10 image window in the stack, were corrected by linearly interpolating
199 translations for adjacent images in the stack. In our data, outlier translations often occur in
200 image slices without any sample present where the lack of image contents limits registration
201 accuracy.
202
203 While a rigid 2D registration approach is sufficient for channel alignment when samples are
204 securely mounted, sporadic movement of some samples during long imaging sessions can
205 result in not only shifting translation but also rotational drift. In these cases, performing
206 registration relying solely on translation will result in only part of the target image aligning
207 correctly to the nuclei reference at a given *z* position with the remaining misaligned target
208 features appearing in *z* positions immediately above and/or below (Figure S1B). To correct for

209   these displacements, we applied a nonlinear 3D registration approach using the Elastix toolbox
210   (Klein et al., 2010) between channels for each individual tile. Full image stacks were loaded and
211   downsampled by a factor of 3 for the *x/y* dimensions to make the volume roughly isotropic and
212   reduce computation time. Intensity histogram matching was then performed and a mask was
213   identified for the nuclei reference channel using an intensity threshold that limits sampling
214   positions in the background. Next, an initial 3D translational registration is performed on the
215   entire image stack between the reference and the remaining channels. The stack is then
216   subdivided into smaller chunks of 300 images and rigid registration is performed on each chunk
217   to account for 3D rotation and achieve a more accurate initial alignment within local regions of
218   the full stack. Finally, a nonlinear B-spline registration is performed on each chunk using an
219   advanced Mattes mutual information metric to account for *xy* drift along the *z* axis and ensure
220   precise alignment of image features. B-spline transformation grid points were set to be sparser
221   along *xy* compared to *z* (800x800x8 voxels) as this setting well balances accurate alignment
222   with computational cost while also preventing local warping of background intensities. To
223   maintain consistency and ensure accurate alignment in all images, the non-rigid alignment
224   method was used for all samples prior to downstream analyses.

225   Iterative Image Stitching

226   A custom 2D iterative stitching procedure was used to assemble whole brain images at high
227   resolution. First, an optimal pairwise *z* correspondence along the axial direction was determined
228   for adjacent tile stacks by exhaustive image matching for the horizontally and vertically
229   overlapped candidate regions. Specifically, a sample of 10 evenly spaced images were taken
230   within a stack and registered to every *z* position within a 20 image window in the adjacent stack
231   using phase correlation. The displacement in *z* with the highest count of peak correlations
232   among the 10 images was presumed to represent the best *z* correspondence. The difference in
233   correlation between the best and the 2nd best *z* displacement was used as a weight for the
234   strength of the correspondence, with a larger difference representing a stronger
235   correspondence. This resulted in 4 matrices: pairwise horizontal and vertical *z* displacements
236   and their corresponding weights. To determine the final *z* displacement for each tile, we
237   implemented a minimum spanning tree (Kruskal, 1956) using displacements and their weights
238   as vertices and edges, as previously implemented (Chalfoun et al., 2017).
239
240   An intensity threshold to measure the amount of non-background signal was determined by
241   uniformly sampling 5% of all images and calculating the median intensity. The starting point for
242   iterative stitching going up/down the stack was selected at a *z* position with non-background
243   signal (set to 1 standard deviation above the darkfield intensity) present in all tiles. Translations
244   in *xy* were calculated using phase correlation and further refined using the Scale Invariant
245   Feature Transform (SIFT) algorithm (Lowe, 2004). The top left tile was set as the starting point
246   for tile placement for each stitching iteration. This ensures stitched images would not be shifted
247   relative to each other along the *z* axis. Tiles were blended using sigmoidal function to maintain
248   high image contrast in overlapping regions. Spurious translations, defined as translations
249   greater than 5 pixels in *x* or *y* from the previous iteration, in images that lacked image content
250   were replaced by translation results from the previous iteration.

Image Registration to ARA Using Point Correspondence

251

252 Volumetric image registration was performed using Elastix to measure the correspondence
253 between the stitched TO-PRO-3 channel in the tissue cleared samples and the Nissl-stained
254 Allen Reference Atlas (ARA) (Dong, 2008; Lein et al., 2007). The atlas and corresponding
255 volume annotations from Common Coordinate Framework v3 were downloaded using the Allen
256 Software Development Kit (SDK) (https://allensdk.readthedocs.io/) at 10 µm/voxel resolution. In
257 each registration procedure, the ARA was downsampled to 25 µm/voxel resolution to perform
258 registration and the resulting transformation parameters were rescaled and applied to the
259 annotation volume at the native 10 µm/voxel resolution.

260

261 For registration without point guidance, an affine followed by B-spline transformation sequence
262 was applied along 3 resolution levels to each sample using advanced mattes mutual information
263 (MMI) as the sole metric to estimate spatial correspondence (as done previously in (Renier et al.
264 2016). For points-guided registration, we first manually placed 200 landmarks within both the
265 ARA and our to-be-registered nuclei reference image, using the BigWarp plugin in Fiji (Bogovic
266 et al., 2016). The majority of points were located within or around the cortex, as this was our
267 region of interest and contained the largest deformations in the *Top1* cKO samples (Figure S4).
268 The same set of reference point coordinates in the ARA were selected for each sample and
269 used as input points in Elastix for affine and B-spline registration along 3 resolution levels.
270 Estimates of spatial correspondence for points-guided registration was driven by a hybrid metric
271 based on (1) minimizing the point distances between two images and (2) maximizing the voxel-
272 wise image similarity between two images which is measured by mattes mutual information
273 (MMI). For affine registration, voxel-wise similarity (based on MMI) was ignored and only points
274 distance was used to estimate global translation, rotation, and scaling transformations. For B-
275 spline registration, we gradually increased the influence of voxel-wise similarity in the hybrid
276 metric during the registration sequence from coarse to fine resolution (1:0.2, 1:0.4, 1:0.6;
277 MMI:Point Distance weight). The inverse of the final transformation parameters was then
278 calculated using a displacement magnitude penalty cost function (Metz et al., 2011) and applied
279 to the Allen Mouse Brain Common Coordinate Framework v3 annotation volume to assign
280 anatomical labels for each voxel in the native sample space. While a more direct approach
281 would be to register the ARA to the sample, we found that registering the sample to the ARA
282 and calculating the inverse achieved slightly higher accuracy in *Top1* cKO brains (data not
283 shown). For WT samples, we registered directly to the ARA without point guidance as we found
284 this produced similar accuracy but slightly higher consistency in structure volumes between
285 samples (Figure S3).

286

287 To evaluate registration accuracy, 3D masks of the entire isocortex were manually labeled for
288 each sample in Imaris (Bitplane) using the 3 acquired channels as markers to delineate cortex
289 boundaries. Some cortical subplate structures, such as the claustrum, were included in the final
290 mask as these were difficult to distinguish from the isocortex. The DICE similarity score was
291 then calculated between each mask and all cortical structures in the registered annotation
292 volume (Figure 2B) as a metric of registration accuracy.

Cortical Volume, Surface Area, and Thickness Measurements

293
294 Quantitative measurements for the volume, surface area, and thickness of 43 cortical areas
295 defined in (Harris et al., 2019) and the full isocortex were calculated based on registered
296 annotation volumes. The voxel sums (at 10 um^3/voxel) represent the total volume of each
297 structure. To calculate volumetric displacement for each sample relative to the Allen atlas, the
298 spatial Jacobian was measured for each set of transformation parameters, which ranges from -1
299 to 1, and represents voxel-wise local compression or expansion. Surface area for the isocortex
300 was calculated based on MATLAB's implementation of Crofton's formula (Lehmann and
301 Legland, 2012). The fraction of layer 1 boundary voxels over all boundary voxels was used to
302 determine the area of only the outer cortical surface. This measurement was then further
303 partitioned by the number of layer 1 boundary voxels for each individual structure. To calculate
304 thickness, the center of mass for layer 1 and layer 6b were first calculated for each structure. A
305 cubic spline was then fit to pass through the center of mass of the full volume and the 2 border
306 voxels nearest to layer 1 and 6b centroids. Thickness was then measured based on the arc
307 length of each spline. Average cortical thickness was weighted by the volume contribution of
308 each structure.

Nuclei Detection

309
310 Imaging data for training the 3D-Unet model was acquired from 3 separate imaging experiments
311 of TO-PRO-3 labeled nuclei across 5 different regions from the cortex of 2 WT brains. Images
312 were captured at 0.75x0.75x2.5 μm/voxel for training a high resolution model or 1.21x1.21x4
313 μm/voxel for training a low resolution model. A binary approximation of the nucleus volume was
314 initially pre-traced using the cell detection component of the CUBIC-informatics pipeline
315 (Matsumoto et al., 2019). Specifically, the thresholded Hessian determinant after Difference-of-
316 Gassian filtering was used to create an initial 3D mask of all nuclei in the image. Full images
317 were then divided into patches of 224x224x64 voxels and preprocessed using min/max
318 normalization. The corresponding 3D mask for each nucleus was reduced to its 2D component
319 at the middle z position. Each patch was then manually inspected and corrected for
320 segmentation error or incorrect shapes using BrainSuite v17a (Shattuck and Leahy, 2002) by 1
321 rater (OK) to reduce person-to-person variability. The corrected 2D nuclei masks were then
322 eroded by removing 40% of the outer edge pixels. Each patch was then subdivided into 4
323 smaller patches of 112x112x32 voxels, with 1 out of the 4 patches being withheld for the
324 validation set. The full dataset (training + validation) contained 16 patches at 224x224x64
325 voxels for both the high (14,554 nuclei) and low resolution (53,993 nuclei) models. Nuclei at the
326 edge of an image stack were also included in the training. Manually labeled data are available at
327 https://braini.renci.org/ using the Download Image service.
328
329 A modified 3D-Unet architecture (Çiçek et al., 2016; Isensee et al., 2018) was used to identify
330 the positions of cell nuclei in whole cortex images. We built upon and modified a previous Keras
331 implementation of 3D-Unet for volumetric segmentation in MRI
332 (https://github.com/ellisdg/3DUnetCNN) to detect binary masks of cell nuclei positions. As
333 originally described (Isensee et al., 2018), the 3D-Unet architecture contains a series of context
334 modules during the contracting path that encodes abstract representations of the input image,

335 followed by a series of localization modules on the upscaling path to localize the features of
336 interest (Figure S4A). We similarly used a model with 5 context modules, residual weights, and
337 deep supervision in the localization modules. The network was trained using 32 base filters on
338 image patches of size 112x112x32 voxels with a batch size of 2. Training presumed over ~300
339 epochs using an Adam optimizer with a dropout rate of 0.4 and an initial learning rate 0.002 that
340 was reduced by a factor of 2 for every 10 epochs without the loss improving. Additional image
341 augmentations were implemented during the training to make the model more generalizable.
342 These include random image permutations, image blurring and sharpening, the addition of
343 random noise, and intensity variations along x,y,z dimensions in the image patch. Random
344 scaling was removed as we found that this decreased model performance.
345
346 Nuclei detection accuracy was evaluated using an independent set of 5 images patches of TO-
347 PRO-3- labeled nuclei where the full 3D volume of each nucleus was fully manually drawn with
348 a unique index at 0.75x0.75x2.5 μm/voxel resolution (~3,500 nuclei total). Each patch was
349 sampled from a unique region within 1 WT cortex. Evaluation patches were initially delineated
350 by 4 raters and further refined by 1 rater to reduce between-person variability. We compared our
351 3D-Unet detection method with those used in 2 previously published pipelines for tissue cleared
352 image analysis: ClearMap and CUBIC-informatics (Matsumoto et al., 2019; Renier et al., 2016).
353 For ClearMap, we used voxel size and intensity thresholds after watersheding, as described in
354 the published implementation. Parameters for cell size and intensity were scaled accordingly to
355 achieve the most accurate average cell counting results possible for all the patches tested.
356 Similarly, intensity normalization and Difference-of-Gaussian scaling parameters used in
357 CUBIC-informatics were adjusted according to image resolution. Filtering by intensity and
358 structureness was also performed as described in the previous work (Matsumoto et al., 2019) .
359
360 In our evaluation of nuclei detection, precision is the proportion of nuclei correctly predicted out
361 of all nuclei predictions in an image patch. Precision is therefore calculated by counting the
362 number of cells with multiple predicted centroids in 1 manually labeled nucleus volume as well
363 as false positives cells called in the image background divided by the total number of nuclei
364 detected and subtracting this number from 1. Recall is the proportion of all nuclei instances that
365 were predicted. Recall was therefore calculated by counting the number of manually labeled cell
366 volumes that lacked any predicted cell centroids divided by the total number of cells. The
367 majority of false negative cases were due to touching nuclei. Nuclei whose centroid were within
368 3 voxels of the image border were excluded from the evaluation.
369
370 Whole brain TO-PRO-3 images were divided into chunks of 112x112x32 voxels to be fed into
371 the trained 3D-Unet model for prediction of cell centroids. An overlap of 16x16x8 voxels was
372 used between adjacent chunks to minimize errors from nuclei at chunk edges. Centroid
373 positions falling in a region less than half the overlap range (i.e. <8 pixels from xy border or <4
374 pixels from z border) were assumed to be counted in the adjacent overlapping chunk and were
375 removed. Additionally, a nearest neighbor search using kd-trees (Bentley, 1975) was performed
376 to remove duplicate centroids within 1.5 voxels of each other, ensuring centroids in overlapping
377 regions were not counted multiple times. Increasing overlap did not significantly affect the final

378 cell counting results (data not shown). Total computation time for detecting all cortical nuclei in 1
379 WT brain hemisphere was ~2.5 hours using a single GPU.

380 ## Cell-type Classification

381 To classify cell-types, we took a supervised approach by training a linear Support Vector
382 Machine (SVM) classifier using MATLAB's Statistics and Machine Learning Toolbox on a set of
383 intensity, shape, and annotation features within a 2D patch surrounding each centroid. First,
384 channel intensities were measured at centroid positions for each channel. Cells with intensities
385 below the median for both Ctip2 and Cux1 were presumed negative for both markers and
386 removed from model training and classification (~25% of cells). In the remaining cells, we took a
387 uniform, random sample of 1,000 cells from each brain image dataset and retained 2D patches
388 (13x13 pixels) around centroid positions. Manual classification required >1 hour per dataset
389 using a custom NuMorph function that allows fast navigation between cell patches. For each
390 patch, we recorded several intensity measurements (max, mean, standard deviation, middle
391 pixel, middle pixel/edge pixel) and applied Otsu thresholding to capture shape measurements
392 (total filled area, inner filled area) in each channel. These were also combined with categorical
393 annotations for cortical layer (L1, L23, L4, L5, L6a, L6b) and cortical area (Prefrontal, Lateral,
394 Somatomotor, Visual, Medial, Auditory; defined in (Harris et al., 2019). Cells were then manually
395 classified into 4 classes: (1) Ctip2-/Cux1-, (2) Ctip2+/Cux1-, (3) Ctip2-/Cux1+, (4) Outlier. The
396 outlier class was annotated according to 4 additional subdivisions due to differences in intensity
397 features: (1) Ctip2+/Cux1+, (2) Pial surface cell, (3) TO-PRO-3-/Ctip2-/Cux1- (4) Striatal cell
398 (only present in *Top1* cKO from residual registration error near white matter boundary). The
399 SVM model was then trained using all intensity, shape, and annotation features. Model
400 accuracy was evaluated using 5-fold cross-validation and applied to the remaining cells for
401 classification. Due to differences in labeling intensity between samples, we trained a new model
402 for each sample instead of aggregating annotation data.
403
404 We compared supervised cell classification with an unsupervised approach based on modeling
405 fluorescence intensities at centroids positions as Gaussian mixtures (GM) for Ctip2 and Cux1.
406 After Z normalization, high intensity cells (Z > 5 and Z < -5) winsorized and outliers expressing
407 both markers near the sample edge were removed. GM model fitting was then performed
408 separately on normalized Ctip2 and Cux1 intensities using 2 or 3 components (whichever had
409 higher accuracy by visual inspection) for 20 replicates using parameters initialized by k-
410 means++ (David Arthur, 2007). Due to spatial variation in gene expression, we stratified GM
411 model fitting to 6 general areas defined in (Harris et al., 2019) according to each cell's structural
412 annotation to further improve accuracy. We then calculated posterior probabilities of each cell
413 being positive for either marker. Cells with a posterior probability greater than 0.5 of not being
414 background were classified as positive. As the vast majority of neurons do not co-express Ctip2
415 and Cux1 (Molyneaux et al., 2007), we filtered Ctip2+/Cux1+ cells according to their layer
416 annotation. Cells in L1-L4 with P(Cux1) > P(Ctip2) were classified as Cux1+ and cells in L5-L6b
417 with P(Ctip2) > P(Cux1) were classified as Ctip2+. The remaining Ctip2+/Cux1+ cells were
418 classified as outliers.

419 Quantification, Statistical Analysis, and Visualization

420 Final cell-type counts were summed for each annotation in the cortex according to its structure
421 tree hierarchy. In our analysis, we chose to compare either 43 cortical areas defined in (Harris
422 et al., 2019) or a more broad grouping of 16 regions at the previous level in the structure
423 hierarchy. Statistics, including mean counts, standard deviation, fold change, raw p values, and
424 false discovery rate (FDR) adjusted p values (Benjamini-Hochberg; FDR < 0.05), were
425 calculated in MATLAB and exported for plotting using custom R scripts and customized slice
426 visualization. Structure volumes were also used to calculate cell density statistics. Unless stated
427 otherwise, descriptive statistics in the main text and error bars in figure plots represent mean ±
428 standard deviation.
429
430 2D slice visualizations were created using a custom MATLAB program based on the
431 allenAtlasBrowser in the SHARP-Track tool (Shamash et al., 2018). Structure annotations were
432 downsampled along the anterior-posterior axis to reduce memory overhead for smoother
433 performance and colored by volume, cell count, or cell density statistics. Additional
434 visualizations for point clouds and surface volumes were created using custom MATLAB scripts
435 and are available in the NuMorph package. Additional animations were generated in Imaris
436 (Bitplane) after importing cell centroid position as "spots" objects.

437 Spatial Gene Expression Correlation

438 Fold change in cell counts between WT and *Top1* cKO were correlated with spatial gene
439 expression based on *in situ* hybridization measurements from the Allen Mouse Brain Atlas (Lein
440 et al., 2007). Expression grid data from sagittal and coronal sections were downloaded using
441 the Allen SDK. Expression energy for each gene was first Z-scored across all brain structures
442 and cortical regions were retained for analysis. Duplicate sections for the same gene were
443 combined by taking the mean Z score for each structure across sections. We filtered out any
444 gene that did not have expression data in all cortical structures and removed genes with Z
445 scores less than 1 in all structures as these represent genes with consistently low cortical
446 expression or with low congruence between duplicate sections. For the remaining genes, we
447 applied a robust sigmoidal transformation as described in (Fulcher and Fornito, 2016) to
448 account for the presence of outliers in ISH expression data. As certain cortical regions also have
449 greater cell density and therefore greater total ISH energy, we conducted an additional Z score
450 normalization across cortical regions to have the same average total gene expression.
451
452 To reduce known false positive associations from gene-gene coexpression (Fulcher et al.,
453 2020), we ran comparisons to ensemble-based random null models generated using the Gene
454 Category Enrichment Analysis toolbox
455 (https://github.com/benfulcher/GeneCategoryEnrichmentAnalysis). Null distributions were
456 generated for GO categories containing between 10 and 200 genes by 10,000 random samples
457 to create a Gaussian distribution estimate of each GO null distribution. In total, we used null
458 models for 4,186 GO categories based on expression of 10,945 genes across 38 cortical
459 structures. Correlations between spatial gene expression and relative cell count differences
460 were tested and corrected for multiple-hypothesis testing using a false discovery rate of 0.05.

461 Additional annotations for gene length comparisons were downloaded from Ensembl
462 (Cunningham et al., 2019). The Spearman correlation between each gene's expression and cell
463 count or density differences across cortical regions was measured and binned by gene length
464 based on the longest isoform for each gene. The mean and standard deviation of all correlation
465 coefficients in each bin (<100kb or >100kb) was used to compare correlation coefficients
466 between bins (Welch's t-test). A list of differentially expressed genes in *Top1* cKO cortex as
467 measured by scRNA-seq was acquired from (Fragola et al., 2020) for additional comparisons.

468 Data and Code Availability

469 NuMorph source code is available at https://bitbucket.org/steinlabunc/numorph/. Manually
470 labeled annotations for 3D-Unet training and raw light-sheet images are available at
471 https://braini.renci.org/ through the "Download Image" service.

472 # Results

473 ## iDISCO+ Reveals Neuronal Cell-type Deficits in the *Top1* cKO Cortex

474 A previous study demonstrated that deletion of *Top1* in postmitotic excitatory neurons within the
475 cortex and hippocampus results in massive neurodegeneration in these structures by postnatal
476 day 15 (P15) (Fragola et al., 2020). Interestingly, while all cortical layers were affected by *Top1*
477 deletion, the lower cortical layers (Layers 5-6) showed a noticeably greater reduction in
478 thickness and cell count compared to the upper cortical layers (Layers 2-4) (Fragola et al.,
479 2020). These observations however were limited to the somatosensory cortex, which itself is a
480 large structure that can be further decomposed into multiple functional regions. To evaluate the
481 effects of *Top1* deletion on excitatory neuron cell-types throughout all cortical structures, we
482 performed iDISCO+ (Renier et al., 2016) to clear and image the *Top1* cKO
483 (*Neurod6$^{Cre/+}$::Top1$^{fl/fl}$*) mouse. We chose to use iDISCO+ among other tissue clearing
484 techniques due to its demonstrated compatibility with antibody labeling, minimal tissue
485 expansion or shrinkage, and simplified protocol (Renier et al., 2016). To go beyond qualitative
486 evaluation, we proceeded to develop cell detection and image registration tools that could
487 accurately quantify the number of upper layer and lower layer neurons in each cortical region in
488 *Top1* cKO mice (Figure 1A).
489
490 We processed one brain hemisphere from four wild-type (WT) and four *Top1* cKO mice at P15 -
491 when the *Top1* cKO had displayed strong, bilateral deficits in brain structure (Fragola et al.,
492 2020). We labeled layer-specific cell-types using antibodies for Cux1 (upper layer neuron
493 marker) and Ctip2 (lower layer neuron marker) in addition to staining all cell nuclei with TO-
494 PRO-3 (TP3) during iDISCO+ processing. After clearing, samples were imaged using the
495 Ultramicroscope II - one of the most widely used commercial light-sheet microscopes for
496 imaging cleared tissues (Cai et al., 2019; Ertürk et al., 2012; Kirst et al., 2020; Liebmann et al.,
497 2016; Pan et al., 2016; Renier et al., 2016; Susaki et al., 2015; Tainaka et al., 2014; Ye et al.,
498 2016). The *Top1* cKO hemispheres displayed a noticeable reduction in overall cortical volume
499 (Figure 1B). During light-sheet imaging, there is a well known trade off between optical
500 resolution, particularly in the axial (*z*) dimension, and imaging speed. While the Ultramicroscope

12

501 ll features axial sweeping to maintain relatively even z resolution throughout the field of view
502 (Dean et al., 2015), the additional mechanical movement of the light-sheet significantly reduces
503 the imaging rate. After testing various imaging schemes, we imaged at 1.21x1.21x4 (µm/voxel)
504 resolution with a light-sheet thickness of 9 µm. The resulting images provided sufficient
505 resolution to visually delineate cell nuclei in the cortex (Figure 1C) while limiting imaging time to
506 ~20 hours for all 3 channels in 1 WT hemisphere (~12 hours for *Top1* cKO).
507
508 Prolonged imaging of cleared tissue samples can induce several artifacts over the course of
509 image acquisition. In particular, drift in the sample or aberrant microscope stage movement can
510 cause misalignment between image tile positions within and between channels. These issues
511 become more pronounced at higher optical resolution where slight variations can prevent
512 colocalization of cell nuclei with their respective immunolabeled markers. To ensure correct
513 alignment between channels, we applied a series of rigid and non-rigid registration steps using
514 the Elastix toolbox (Klein et al., 2010) to map the Cux1 and Ctip2 channels onto the TO-PRO-3
515 channel without inducing non-specific local background warping (Figure S1). We also found that
516 many of the commonly used programs for performing 3D image stitching (Bria and Iannello,
517 2012; Hörl et al., 2019) did not accurately align adjacent tile stacks due to spurious stage
518 movement, which has been noted by other groups (Kirst et al., 2020). To ensure accurate image
519 reconstruction, we applied a simplified iterative 2D stitching procedure that uses scale-invariant
520 feature transforms (Lowe, 2004) to produce continuous images without cell duplication along tile
521 edges (Figure S2). Finally, differences in fluorescence intensity caused by light attenuation and
522 photo bleaching during the course of imaging can result in uneven brightness between image
523 tile positions. To ensure uniform signal across tiles, we measured the differences in image
524 contrast in overlapping tile regions to estimate and correct for variations in signal intensity
525 among tile stacks (Figure S1D).
526
527 Completion of the preprocessing steps described above resulted in aligned, fully stitched 3
528 channel images and datasets <1TB per sample (~360GB for WT and ~170GB for *Top1* cKO).
529 The *Top1* cKO hemispheres displayed clear reductions in thickness throughout the cortex
530 (Figure 1D). While all cortical layers showed some amount of degeneration, Layer 5 and Layer 6
531 neurons seemed to be more severely depleted (Figure 1E) and we hypothesized that certain
532 cortical areas may be differentially impacted as well.
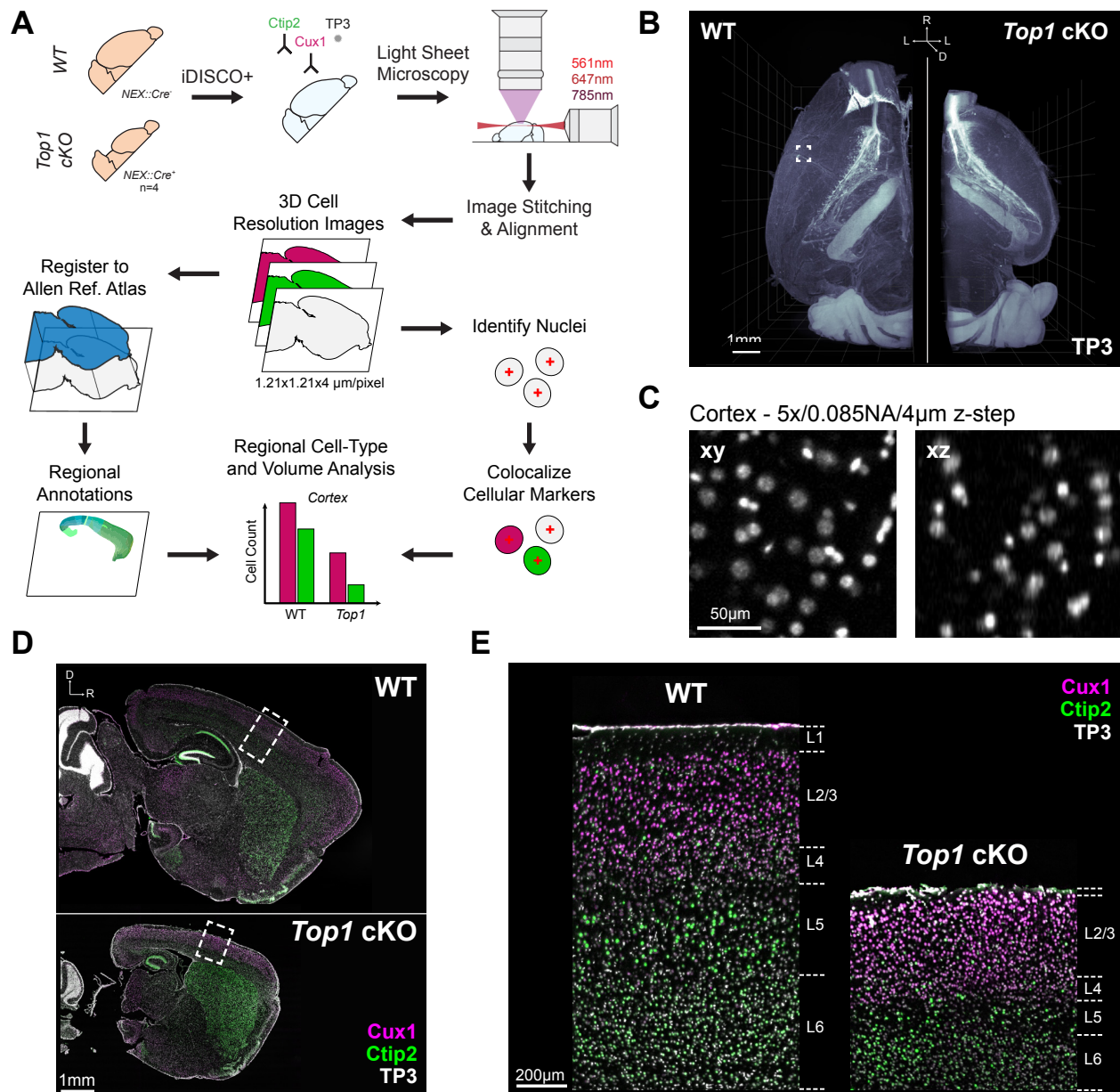
Figure 1. Cellular Resolution Analysis of Brain Structure Phenotypes for Tissue Cleared 3D Brain Images.

A. Overview of tissue processing, imaging, and image analysis procedures. B. 3D rendering of cell nuclei in WT and *Top1* cKO samples. C. Example of TO-PRO-3 (TP3) labeled nuclei within WT cortex captured at sufficient lateral (*xy*) and axial (*xz*) resolution for cell quantification. D. Sagittal sections of TO-PRO-3 nuclear staining and immunolabeling for cell-type specific markers Ctip2 (lower layer neuron) and Cux1 (upper layer neuron) in WT and *Top1* cKO samples. E. Zoomed in images of boxed cortical areas in D demonstrating channel alignment and showing the expected localization of upper and lower layer markers.
Scale: 1 mm (B,D), 50 μm (C), 200 μm (E).

14

543 Point Correspondence Improves Image Registration for Structures with Large
544 Morphological Differences

545 Because of the significant differences in gross morphology within the *Top1* cKO brain, image
546 registration was not accurate using only intensity-based mutual information metrics (Figure 2A).
547 To improve registration accuracy of the *Top1* cKO brain, we manually selected up to 200 points
548 at distinguishable structure landmarks in the Nissl stained ARA and their corresponding
549 locations in the TO-PRO-3 nuclei channel for each sample. Point locations were positioned
550 primarily around the cortex as this was our region of interest (Figure S3). Using Euclidean point
551 distances as an additional metric during the registration process significantly improved cortical
552 annotation when compared to a manually delineated mask (Figure 2A). Increasing the number
553 of points resulted in higher DICE similarity coefficient scores in *Top1* cKO samples (*Top1* cKO
554 MMI, mean = 0.526, s.d. = 0.189; *Top1* cKO MMI + 200 Pts, mean = 0.890 s.d. = 0.013)
555 indicating improvements in registration accuracy (Figures 2B and S3C). These results show that
556 point correspondence can be used to better register mouse models with large structural
557 variation.
558
559 Using the spatial deformation fields generated after image registration, we analyzed which
560 areas in the *Top1* cKO cortex exhibited the largest changes in volume relative to WT. While the
561 cortex as a whole showed a large reduction in volume (mean = 80%, s.d. = 3.7%, p < 0.001),
562 we observed slightly greater decreases in frontal regions, such as the orbitofrontal (ORB) and

15
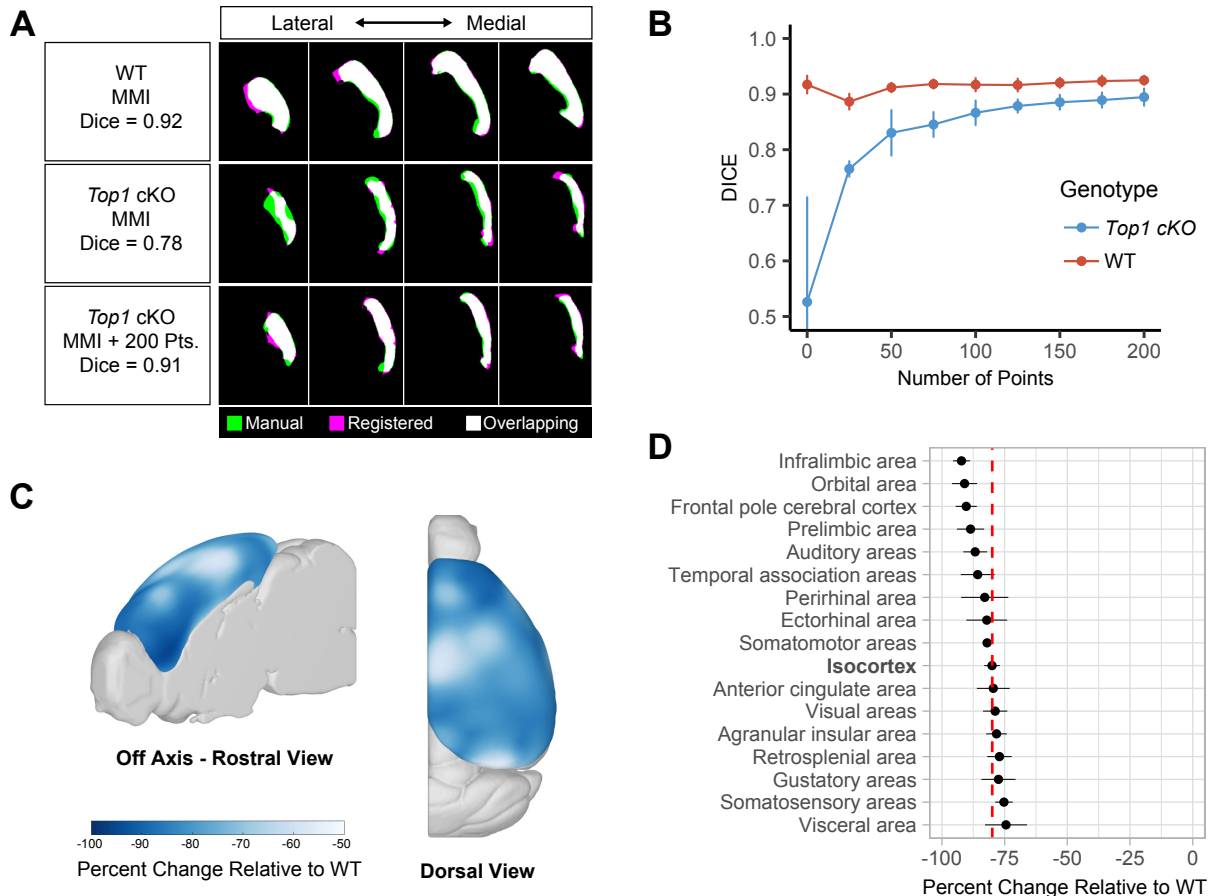
Figure 2. Improved Image Registration Using Corresponding Points Identifies Region-Specific Deficits.
A. Cortical masks from registered WT and *Top1* cKO brain images (Magenta) compared with manual labelled traces (Green). Mattes mutual information (MMI) was used as the primary registration metric with additional point correspondence to guide registration in the *Top1* cKO case. B. DICE scores measuring cortical registration accuracy in WT and *Top1* cKO samples based on the number of points used to guide registration. Measurements with no corresponding points were made using affine + b-spline registration without a points distance metric. Data represented as mean ± standard deviation. C. Voxel-wise differences in cortical volumes between *Top1* cKO and WT samples. D. Percent change in cortical region volumes in *Top1* cKO samples compared to WT. Dashed line indicates average change in the entire cortex. Data represented as mean ± SEM.

infralimibic (ILA) areas, as well as certain lateral regions near the temporal association area (TEa) (Figures 2C and 2D). This suggests that the neuronal cell-types within these structures may be more susceptible to degeneration upon *Top1* deletion.

3D-Unet Accurately Quantifies Cell Nuclei in the Cortex

3D cell segmentation of tissue cleared images can be difficult due to the density of cells in the brain, limits of imaging resolution, and overall data complexity. Here we implemented a deep learning model, based on a 3D version of the popular U-Net framework (3D-Unet) (Çiçek et al., 2016; Isensee et al., 2018), to accurately quantify the total number of cell nuclei marked by TO-PRO-3 staining within the cortex. We generated two sets of manually labeled nuclei: (1) For training, ~67,000 cortical nuclei were manually delineated from 256 training image patches (112x112x32 voxels/patch) of cortical nuclei at either high (0.75x0.75x2.5 µm/voxel) or low (1.21x1.21x4 µm/voxel) spatial resolutions. To increase manual delineation efficiency, we focused only on cell detection by delineating a 2D binary mask at the middle Z position to be used as a marker for each cell nucleus. (2) For evaluation, an independent set of ~3,500 manually delineated nuclei were used where the full 3D extent of the nucleus was labeled in order to determine accuracy of predicted centroid placement. Cell marker predictions within each 3D patch were then thresholded and analyzed for connected components to calculate final cell centroid positions (Figure 3A).

Using the trained 3D-Unet model, we counted 8.43(± 0.05)x10^6 cells in the P15 WT cortex (Figure 3B), which was similar to previously published results in adult mice (Murakami et al., 2018). To evaluate cell detection accuracy, we compared precision and recall rates for detecting nuclei in the evaluation dataset using 3D-Unet and two previously published analysis tools for tissue cleared images with cell counting components: ClearMap and CUBIC Informatics (CUBIC). In our tests, 3D-Unet achieved the highest precision and recall rates in both high and low resolution images when the full training datasets were used (Figures 3C and 3D). At low resolution, 3D-Unet achieved significantly lower error rates compared to the next best performing method (CUBIC) at higher resolution ($p = 0.043$, CUBIC 0.75/3D-Unet 1.21; $p < 0.001$, CUBIC 1.21/3D-Unet 1.21; $p < 0.001$, ClearMap 1.21/3D-Unet 1.21; McNemar's test). This indicates that, with sufficient training, deep neural networks can compensate for a lack of imaging resolution and achieve accurate cell quantification.

16
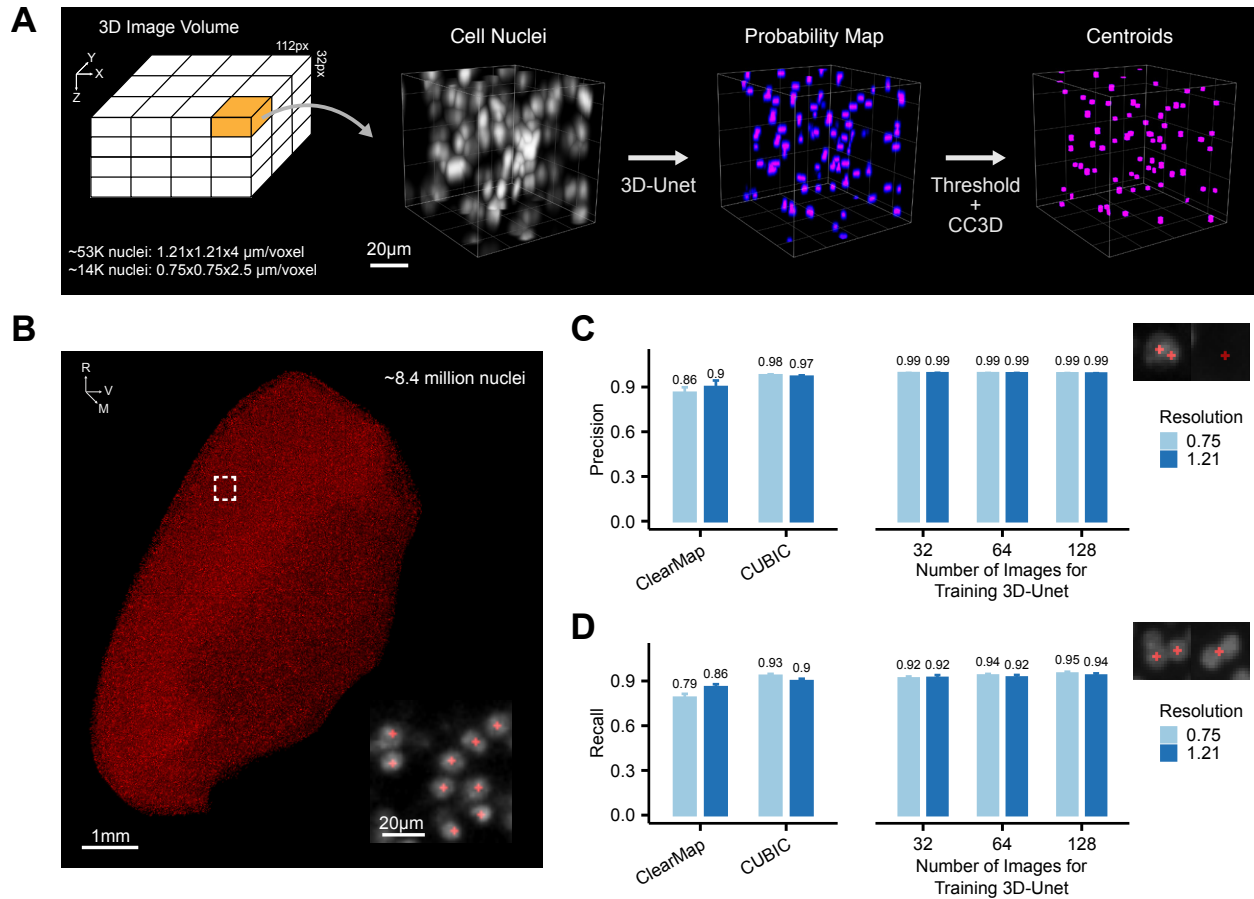
607
Figure 3. Cell Detection Using 3D-Unet Shows Improved Accuracy Compared to Non-learning Based Methods.
610 A. Description of 3D-Unet approach for detecting cell centroids (CC3D: 3D Connected Component Analysis). B. Cell centroids of WT cortical nuclei predicted by 3D-Unet. C-D. Comparison of cell detection precision (C) or recall (D) at the indicated *xy* resolutions (μm/pixel). Examples of misclassification instances contributing to false positive errors (C) or false negative errors (D) are shown above. Data represented as mean ± standard deviation.

615

616 Lower Layer Neurons in the Frontal Cortex Are Preferentially Targeted by *Top1* Deletion

617 To quantify neuronal cell-types in WT and *Top1* cKO cortexes, we developed a supervised Support Vector Machine (SVM) model to classify cell-types based on local intensity, shape, and annotation features. We found that a supervised approach, after training on 1,000 nuclei in each brain sample, achieved more accurate classification compared to an unsupervised mixture model approach (Figure S5). After removing outliers and summing across cortical structures, we counted $1.74(\pm 0.07)\times10^6$ Ctip2+ and $1.95(\pm 0.05)\times10^6$ Cux1+ in WT compared to $0.30(\pm 0.08)\times10^6$ Ctip2+ and $0.73(\pm 0.11)\times10^6$ Cux1+ in the *Top1* cKO (Figures 4A and 4B). Overall, this constitutes an ~83% decrease in Ctip2+ cells and ~62% decrease in Cux1+ cells. When compared to previous results in 2D sections from somatosensory cortex (Fragola et al., 2020), we saw a similar bias towards lower layer neuron degeneration (Cux1/Ctip2 = 1.97 in 3D SSp; 2.33 in 2D), however with a larger reduction in total neuron counts. While this can be partially

628 attributed to differences in cell quantification methods, the increase in sampling depth from
629 volumetric analyses can also uncover larger effects in total cell count compared to serial 2D
630 analysis.
631
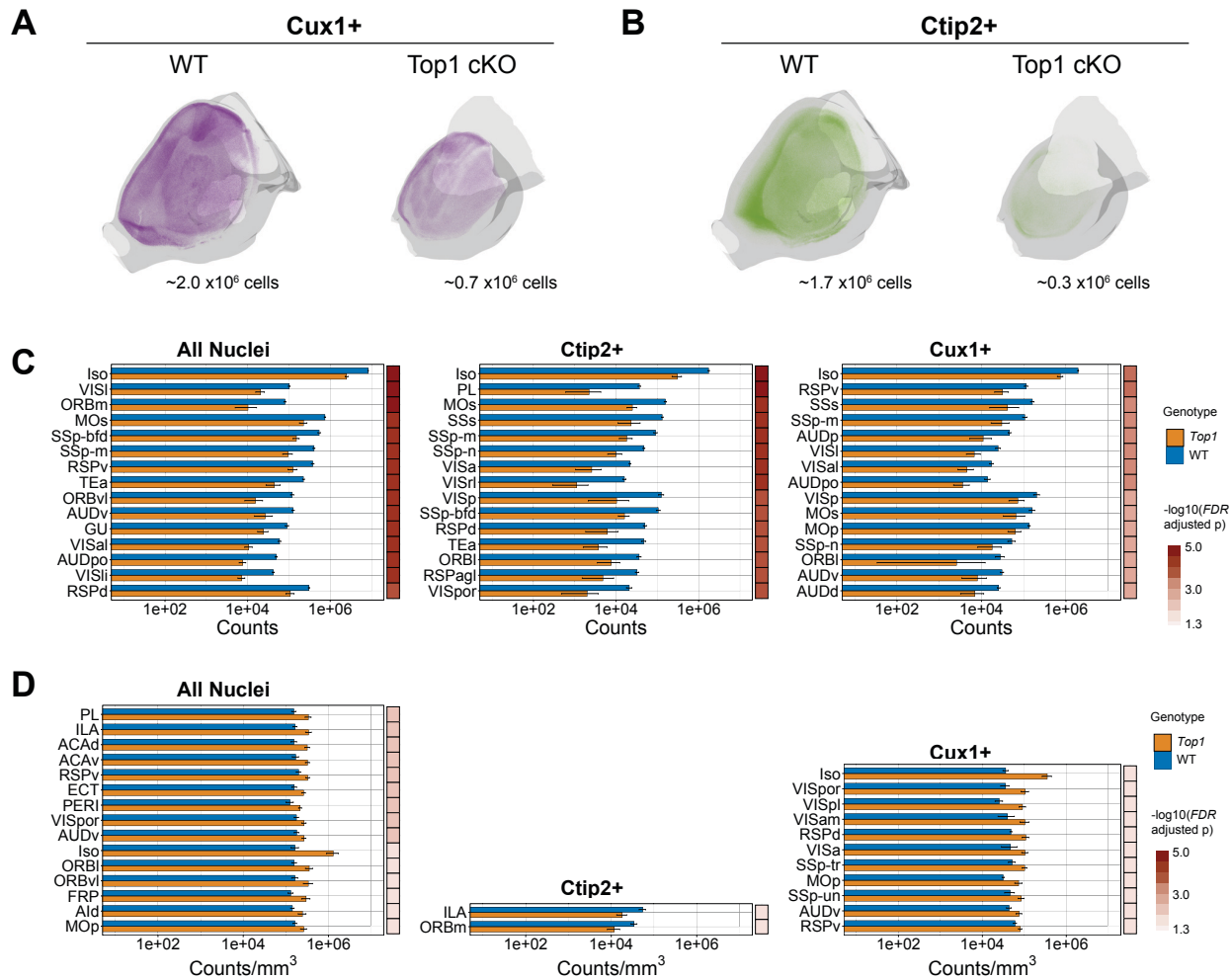
Figure 4. *Top1* Deletion Induces Broad Degeneration of Neuronal Cell-types but Increases Cell Density.
A-B. Point cloud display of Cux1+ (A) or Ctip2+ (B) cells within WT and *Top1* cKO cortexes.
C-D. Comparison of cell-type counts (C) or densities (D) between WT and *Top1* cKO across cortical regions and the full isocortex. Displaying the top 15 structures (FDR < 0.05) binned by significance level and sorted by absolute difference in count or density within each bin. Data represented as mean ± standard deviation and plotted on log$_{10}$ scale. Structure name abbreviations provided in Table S1.

641 Next, we compared differences in cell counts and density for 43 cortical areas defined by
642 functional connectivity in the ARA (Harris et al., 2019) and the complete isocortex to see which
643 regions were most affected by *Top1* deletion. After correcting for multiple comparisons (FDR <
644 0.05), all but one of the 43 structures showed a significant decrease in total TO-PRO-3 cell
645 count indicating broad degeneration across all cortical areas in the *Top1* cKO model (Figure 4C
646 and 5). Among neuronal cell-types, we identified 25 and 41 structures with significant decreases

647   in Cux1+ and Ctip2+ cell counts, respectively. While many structures, including several areas in
648   somatosensory cortex (SSp-n, SS-m, SSp-bfd), shared significant losses in both Cux1+ and
649   Ctip2+ excitatory neurons, the largest reductions were seen in Ctip2+ cells localized in frontal
650   areas, such as the prelimbic area (PL) and secondary motor area (MOs) not measured in
651   previous work (Fragola et al., 2020). We then calculated cell density by normalizing counts to
652   registered structure volumes. Interestingly, the majority of structures show significant increases
653   in TO-PRO-3+ cell density (Figure 4D), suggesting that, in addition to cell loss, degeneration of
654   neuronal processes is also contributing to differences in cortical structure. Structures with the
655   largest increases were again localized in frontal regions, such as the prelimbic (PL), infralimbic
656   (ILA), and orbitofrontal (ORB) areas, as well as medial regions, such as the anterior cingulate
657   areas (ACA). Decreases in cell number also resulted in greater reductions in cortical surface
658   area compared to cortical thickness (Figure S6). Taken together, these results show that, even
659   in cases where genetic perturbation induces strong phenotypic effects such as in the *Top1* cKO
660   model, NuMorph can reveal more localized differences in cell-type number within specific brain
661   regions.

662
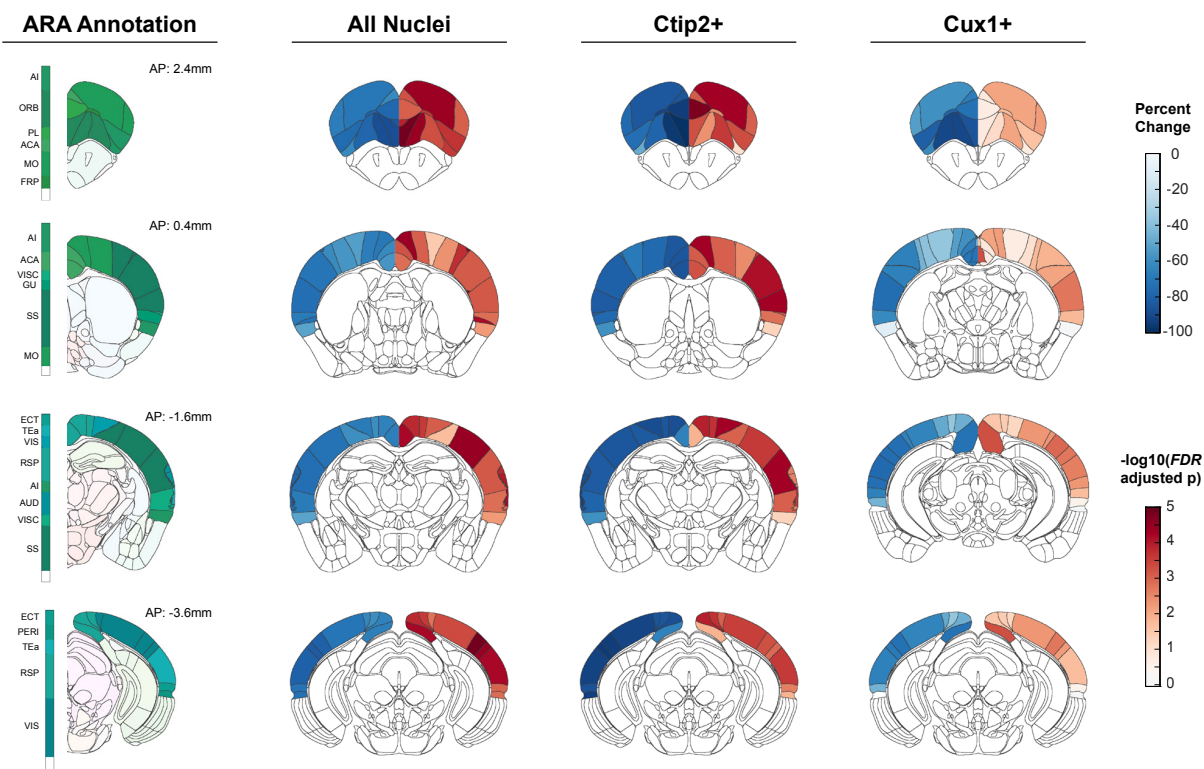
663   **Figure 5. Effects of *Top1* Deletion Vary Across Cortical Structures and Cell-types.**
664   Coronal slice visualizations displaying percent change in cell count (left hemisphere) and FDR-
665   adjusted p values (right hemisphere) from (Figure 4C). Colored ARA annotations at
666   corresponding positions displayed for reference.

19

667 **Neurodegeneration is Spatially Correlated with Genes Differentially Expressed in *Top1***
668 **cKO**

669 Previous evidence suggests that lower layer neurons, particularly those in L5, are most
670 susceptible to degeneration as a result of reduced expression of long, neuronal genes in the
671 *Top1* cKO model (Fragola et al., 2020). While the severe structural deficits in *Top1* cKO
672 precluded us from accurately quantifying L5 neurons in individual cortical regions, we found that
673 regions with large L5 volumes in the ARA saw the greatest reductions in total structure volume
674 in *Top1* cKO (Figure 6A). Furthermore, these regions also saw the largest increases in cell
675 density (Figure 6B) suggesting local degeneration of neuronal processes. We then performed
676 spatial correlations between regional cell count differences and gene expression using in-situ
677 hybridization (ISH) data from Allen Mouse Brain Atlas (AMBA) (Lein et al., 2007). We tested
678 whether the degree of *Top1* cKO induced structural change among cortical regions was related
679 to the expression of long genes (i.e. genes >100kb) within those regions, as *Top1* is known to
680 be a transcriptional regulator of long genes (King et al., 2013; Mabb et al., 2016). We found that
681 in WT, regions with higher densities of Ctip2+ lower layer neurons were significantly associated
682 with increased long gene expression (Figure 6C), providing further support that lower layer
683 neurons express longer genes. Additionally, regions with larger reductions in cell numbers in
684 *Top1* cKO were correlated with increased long gene expression (Figure 6D). Interestingly, fold
685 change in Ctip2+ count differences saw the lowest positive correlation, likely because significant
686 lower layer degeneration had already occurred by P15, minimizing variation between individual
687 cortical regions. Gene Ontology analysis using random-null ensembles to overcome gene-
688 enrichment bias (Fulcher et al., 2020), identified 113 functional annotations associated with
689 greater neuronal loss, including several processes involved in axon guidance and extension
690 (Figure S6D). We then searched for spatial correlations with individual genes differentially
691 expressed in the P7 *Top1* cKO cortex as measured by scRNA-seq (Fragola et al., 2020).
692 Among the 125 differentially expressed genes in *Top1* cKO that also contained ISH signatures
693 in the AMBA, 5 were significantly correlated with relative difference in excitatory neuron count
694 (Figure 6E). The most signficant gene, S100a10 (also known as p11), is predominantly
695 expressed by L5a corticospinal motor neurons in the cortex (Arlotta et al., 2005; Milosevic et al.,
696 2017). Large reductions in Ctip2+ neurons in the *Top1* cKO secondary motor area (MOs) and
697 other frontal areas where S100a10 is highly expressed, suggest that changes in S100a10
698 expression may increase susceptibility for L5 degeneration in these regions (Figures 6F and
699 6G). These results demonstrate how existing spatial gene expression resources can be
700 leveraged with cleared tissue analysis to identify the specific genes, cell-types, and biological
701 processes contributing to gene-structure associations.
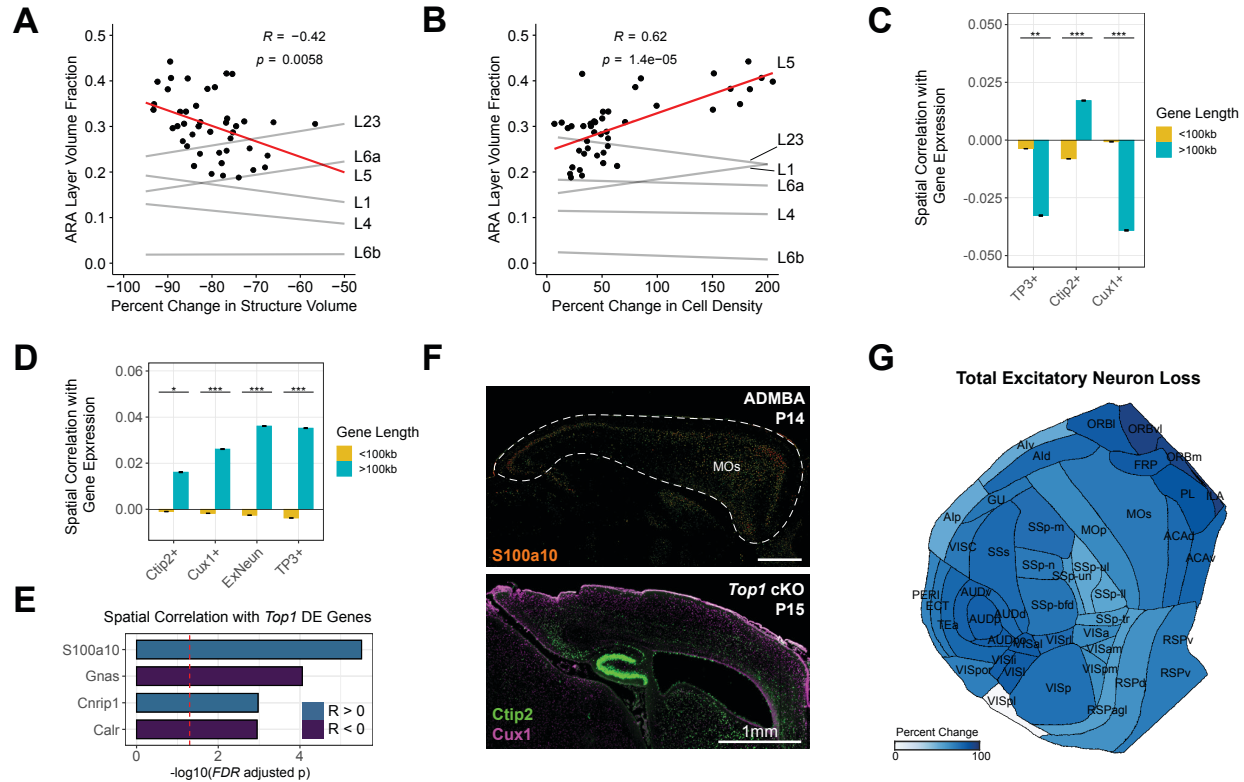
Figure 6. Effects of *Top1* Deletion Are Associated with Spatial Patterns of Gene Expression.

A-B. Association between structure volume (A) and cell density (B) in *Top1* cKO with L5 volume as a fraction of total volume in the ARA. (R: Spearman correlation coefficient). C-D. Association between spatial gene expression and WT cell density (C) or negative fold change in cell count between *Top1* cKO and WT (D). Spearman correlation coefficients, binned by gene length, for each gene's expression across cortical regions were used for comparisons. Increased correlation indicates stronger association with cell loss in (D). TP3+ indicates all cells and ExNeun indicates excitatory neurons (i.e. Ctip2+ or Cux1+). Displaying mean ± SEM. E. Genes differentially expressed in *Top1* cKO excitatory neurons significantly correlated with relative change in excitatory neuron count across cortical regions (Spearman; FDR < 0.05). F. ISH expression of S100a10 at P14 in the Allen Developing Mouse Brain Atlas (ADMBA) with the cortex outlined and a corresponding sagittal section of *Top1* cKO. (MOs: secondary motor area). G. Flattened isocortex displaying percent change in excitatory neuron counts (i.e. Ctip2+ or Cux1+) in *Top1* cKO relative to WT.

Discussion

Tissue clearing methods provide a unique opportunity to explore the cellular organization of the entire 3 dimensional brain structure. However, the current computational tools for analyzing cell-types in tissue cleared images have either been applied to sparse cell populations where segmentation is less difficult (Renier et al., 2016; Yun et al., 2019) or taken advantage of tissue expansion and custom-built light sheet systems to increase spatial resolution (Matsumoto et al., 2019; Murakami et al., 2018). Here, we present NuMorph, a computational pipeline for

21

724 processing and quantifying nuclei within structures of the adult mouse brain acquired by
725 conventional light-sheet fluorescence microscopy.
726
727 In the course of developing NuMorph and an appropriate imaging protocol, a large emphasis
728 was placed on outlining a reasonable compromise between cell detection accuracy, imaging
729 time, and computational resources. With the imaging parameters used to resolve cortical nuclei
730 in this study, WT brain hemispheres required 5-7 hours of imaging per channel, while end-to-
731 end processing and analysis using NuMorph required ~1 day with a GPU-equipped workstation.
732 By training a 3D-Unet model on a diverse set of manually labeled nuclei from multiple imaging
733 experiments, we were able to achieve effectively equivalent error rates at this resolution
734 compared to 1.6x higher resolution (p = 0.91, 3D-Unet 0.75/3D-Unet 1.21; McNemar's test) that
735 would have otherwise required significantly longer imaging times and expanded data size by
736 ~4x for a whole hemisphere acquisition. We expect cell detection accuracy using the training
737 dataset generated here will remain high for analyzing other brain regions with similar cell
738 density, while supplementation with additional training data may be needed for denser
739 structures such as the hippocampus. Furthermore, NuMorph provides additional features and
740 flexibility such as (1) targeting analyses to specific structures after registration to avoid
741 unnecessary computation time, (2) detecting cells directly by nuclear protein marker expression
742 without DNA staining, and (3) classifying cell-types by cellular markers using either supervised
743 or unsupervised methods.
744
745 Top1 is critical for maintaining genomic stability and regulating the expression of long genes
746 important for neuronal function (McKinnon, 2016). Recent evidence suggests that many of these
747 same long genes contribute to neuronal diversity and have the greatest expression in the
748 forebrain (Sugino et al., 2019). In the developing cortex, scRNA-seq studies found that L5
749 neurons had higher long gene expression compared to neurons from other cortical layers (Loo
750 et al., 2019). In this study, we found that *Top1* deletion preferentially targeted many frontal
751 areas with high L5 thickness, larger numbers of Ctip2+ lower layer neurons, and greater long
752 gene expression. These effects likely occur much earlier than the time point studied here as
753 previous behavioural assays showed that severe motor deficits are present as early as P7
754 (Fragola et al., 2020). Interestingly, inhibition of S100a10 - the gene most correlated with neuron
755 loss - was recently shown to have a neuroprotective effect, delaying motor neuron loss in a
756 mouse model amyotrophic lateral sclerosis (ALS) (García-Morales et al., 2019). Because *Top1*
757 deletion results in multiple stress factors that negatively impact cell health, additional studies will
758 be needed to disambiguate which mechanisms ultimately lead to biased degeneration of certain
759 neuronal subtypes across brain regions.
760
761 While NuMorph has proven to be effective in analyzing moderately dense tissues such as the
762 adult mouse cortex, the development of additional computational tools may be required to
763 pursue more challenging experimental designs. For example, structures in the embryonic brain
764 are typically of much higher cell density and vary in gross morphology across developmental
765 time, making both cell quantification and image registration more difficult. In addition,
766 segmentation and mapping of fine structures, such as neuronal processes, can be challenging
767 with limited imaging resolution. Technological improvements in the next generation of light-sheet

768 systems can ultimately allow for quantitative interrogation of subcellular structures at high
769 throughput (Migliori et al., 2018; Voleti et al., 2019). However, computational tools using deep
770 neural networks have also proven to be effective in executing diverse segmentation tasks
771 (Friedmann et al., 2020; Kirst et al., 2020; Schubert et al., 2019; Stringer et al., 2020) or even
772 enhancing image quality (Weigert et al., 2018). Nevertheless, community-based efforts may be
773 needed to generate sufficient annotation data for training deep learning models to accurately
774 perform these tasks (Roskams and Popović, 2016). Together we hope these new imaging and
775 computational tools will lead to greater adoption of tissue clearing methods for quantitative
776 analyses, rather than qualitative visualizations, of how the entire brain structure is changed by
777 genetic or environmental risk factors for neuropsychiatric disorders.

Author Contributions

790 JLS and OK designed the study. OK performed tissue clearing, imaging, and developed
791 NuMorph for image analysis. GF and MJZ provided fixed mouse brain tissue. OK generated all
792 manual annotations for training the 3D-UNet model. EHF, JM, TL, ZH, and OK performed 3D
793 nuclei volume tracing for evaluating the 3D-Unet model. AK provided computational
794 infrastructure to distribute data and results. GW provided guidance on image processing. JLS
795 supervised the work. OK and JLS wrote the first draft of the manuscript, and all authors
796 provided feedback.

Declarations of Interest

798 The authors declare no conflicts of interest.

References

Arlotta, P., Molyneaux, B.J., Chen, J., Inoue, J., Kominami, R., and Macklis, J.D. (2005). Neuronal subtype-specific genes that control corticospinal motor neuron development in vivo. Neuron *45*, 207–221.

Bentley, J.L. (1975). Multidimensional binary search trees used for associative searching. Commun. ACM *18*, 509–517.

Bogovic, J.A., Hanslovsky, P., Wong, A., and Saalfeld, S. (2016). Robust registration of calcium images by learned contrast synthesis. In 2016 IEEE 13th International Symposium on Biomedical Imaging (ISBI), pp. 1123–1126.

Bria, A., and Iannello, G. (2012). TeraStitcher - a tool for fast automatic 3D-stitching of teravoxel-sized microscopy images. BMC Bioinformatics *13*, 316.

Cai, R., Pan, C., Ghasemigharagoz, A., Todorov, M.I., Förstera, B., Zhao, S., Bhatia, H.S., Parra-Damas, A., Mrowka, L., Theodorou, D., et al. (2019). Panoptic imaging of transparent mice reveals whole-body neuronal projections and skull-meninges connections. Nat. Neurosci. *22*, 317–327.

Chalfoun, J., Majurski, M., Blattner, T., Bhadriraju, K., Keyrouz, W., Bajcsy, P., and Brady, M. (2017). MIST: Accurate and Scalable Microscopy Image Stitching Tool with Stage Modeling and Error Minimization. Sci. Rep. *7*, 4988.

Chen, F., Tillberg, P.W., and Boyden, E.S. (2015). Optical imaging. Expansion microscopy. Science *347*, 543–548.

Çiçek, Ö., Abdulkadir, A., Lienkamp, S.S., Brox, T., and Ronneberger, O. (2016). 3D U-Net: Learning Dense Volumetric Segmentation from Sparse Annotation.

Cunningham, F., Achuthan, P., Akanni, W., Allen, J., Amode, M.R., Armean, I.M., Bennett, R., Bhai, J., Billis, K., Boddu, S., et al. (2019). Ensembl 2019. Nucleic Acids Res. *47*, D745–D751.

David Arthur, S.V. (2007). K-means++: the advantages of careful seeding. In In Proceedings of the 18th Annual ACM-SIAM Symposium on Discrete Algorithms,.

Dean, K.M., Roudot, P., Welf, E.S., Danuser, G., and Fiolka, R. (2015). Deconvolution-free Subcellular Imaging with Axially Swept Light Sheet Microscopy. Biophys. J. *108*, 2807–2815.

Dong, H.W. (2008). The Allen reference atlas: A digital color brain atlas of the C57Bl/6J male mouse. *57B*, 6J.

Ertürk, A., Becker, K., Jährling, N., Mauch, C.P., Hojer, C.D., Egen, J.G., Hellal, F., Bradke, F., Sheng, M., and Dodt, H.-U. (2012). Three-dimensional imaging of solvent-cleared organs using 3DISCO. Nat. Protoc. *7*, 1983–1995.

Fei, P., Nie, J., Lee, J., Ding, Y., Li, S., and Zhang, H. (2019). Subvoxel light-sheet microscopy for high-resolution high-throughput volumetric imaging of large biomedical specimens. Advanced.

Fragola, G., Mabb, A.M., Taylor-Blake, B., Niehaus, J.K., Chronister, W.D., Mao, H., Simon,

836 J.M., Yuan, H., Li, Z., McConnell, M.J., et al. (2020). Deletion of Topoisomerase 1 in excitatory
837 neurons causes genomic instability and early onset neurodegeneration. Nat. Commun. *11*,
838 1962.

839 Friedmann, D., Pun, A., Adams, E.L., Lui, J.H., Kebschull, J.M., Grutzner, S.M., Castagnola, C.,
840 Tessier-Lavigne, M., and Luo, L. (2020). Mapping mesoscale axonal projections in the mouse
841 brain using a 3D convolutional network. Proc. Natl. Acad. Sci. U. S. A. *117*, 11068–11075.

842 Fulcher, B.D., and Fornito, A. (2016). A transcriptional signature of hub connectivity in the
843 mouse connectome. Proc. Natl. Acad. Sci. U. S. A. *113*, 1435–1440.

844 Fulcher, B.D., Arnatkevičiūtė, A., and Fornito, A. (2020). Overcoming bias in gene-set
845 enrichment analyses of brain-wide transcriptomic data.

846 Gao, R., Asano, S.M., Upadhyayula, S., Pisarev, I., Milkie, D.E., Liu, T.-L., Singh, V., Graves,
847 A., Huynh, G.H., Zhao, Y., et al. (2019). Cortical column and whole-brain imaging with molecular
848 contrast and nanoscale resolution. Science *363*.

849 García-Morales, V., Rodríguez-Bey, G., Gómez-Pérez, L., Domínguez-Vías, G., González-
850 Forero, D., Portillo, F., Campos-Caro, A., Gento-Caro, Á., Issaoui, N., Soler, R.M., et al. (2019).
851 Sp1-regulated expression of p11 contributes to motor neuron degeneration by membrane
852 insertion of TASK1. Nat. Commun. *10*, 3784.

853 Goebbels, S., Bormuth, I., Bode, U., Hermanson, O., Schwab, M.H., and Nave, K.-A. (2006).
854 Genetic targeting of principal neurons in neocortex and hippocampus of NEX-Cre mice. Genesis
855 *44*, 611–621.

856 Harris, J.A., Mihalas, S., Hirokawa, K.E., Whitesell, J.D., Choi, H., Bernard, A., Bohn, P.,
857 Caldejon, S., Casal, L., Cho, A., et al. (2019). Hierarchical organization of cortical and thalamic
858 connectivity. Nature *575*, 195–202.

859 Hörl, D., Rojas Rusak, F., Preusser, F., Tillberg, P., Randel, N., Chhetri, R.K., Cardona, A.,
860 Keller, P.J., Harz, H., Leonhardt, H., et al. (2019). BigStitcher: reconstructing high-resolution
861 image datasets of cleared and expanded samples. Nat. Methods *16*, 870–874.

862 Isensee, F., Kickingereder, P., Wick, W., Bendszus, M., and Maier-Hein, K.H. (2018). Brain
863 Tumor Segmentation and Radiomics Survival Prediction: Contribution to the BRATS 2017
864 Challenge.

865 King, I.F., Yandava, C.N., Mabb, A.M., Hsiao, J.S., Huang, H.-S., Pearson, B.L., Calabrese,
866 J.M., Starmer, J., Parker, J.S., Magnuson, T., et al. (2013). Topoisomerases facilitate
867 transcription of long genes linked to autism. Nature *501*, 58–62.

868 Kirst, C., Skriabine, S., Vieites-Prado, A., Topilko, T., Bertin, P., Gerschenfeld, G., Verny, F.,
869 Topilko, P., Michalski, N., Tessier-Lavigne, M., et al. (2020). Mapping the Fine-Scale
870 Organization and Plasticity of the Brain Vasculature. Cell *180*, 780–795.e25.

871 Klein, S., Staring, M., Murphy, K., Viergever, M.A., and Pluim, J.P.W. (2010). elastix: a toolbox
872 for intensity-based medical image registration. IEEE Trans. Med. Imaging *29*, 196–205.

873 Kruskal, J.B. (1956). On the Shortest Spanning Subtree of a Graph and the Traveling Salesman
874 Problem. Proc. Am. Math. Soc. *7*, 48–50.

875   Ku, T., Swaney, J., Park, J.-Y., Albanese, A., Murray, E., Cho, J.H., Park, Y.-G., Mangena, V.,
876   Chen, J., and Chung, K. (2016). Multiplexed and scalable super-resolution imaging of three-
877   dimensional protein localization in size-adjustable tissues. Nat. Biotechnol. *34*, 973–981.

878   Lehmann, G., and Legland, D. (2012). Efficient N-Dimensional surface estimation using Crofton
879   formula and run-length encoding. Efficient N-Dimensional Surface Estimation Using Crofton
880   Formula and Run-Length Encoding, Kitware INC(2012).

881   Lein, E.S., Hawrylycz, M.J., Ao, N., Ayres, M., Bensinger, A., Bernard, A., Boe, A.F., Boguski,
882   M.S., Brockway, K.S., Byrnes, E.J., et al. (2007). Genome-wide atlas of gene expression in the
883   adult mouse brain. Nature *445*, 168–176.

884   Liebmann, T., Renier, N., Bettayeb, K., Greengard, P., Tessier-Lavigne, M., and Flajolet, M.
885   (2016). Three-Dimensional Study of Alzheimer's Disease Hallmarks Using the iDISCO Clearing
886   Method. Cell Rep. *16*, 1138–1152.

887   Loo, L., Simon, J.M., Xing, L., McCoy, E.S., Niehaus, J.K., Guo, J., Anton, E.S., and Zylka, M.J.
888   (2019). Single-cell transcriptomic analysis of mouse neocortical development. Nat. Commun.
889   *10*, 134.

890   Lowe, D.G. (2004). Distinctive Image Features from Scale-Invariant Keypoints. Int. J. Comput.
891   Vis. *60*, 91–110.

892   Mabb, A.M., Simon, J.M., King, I.F., Lee, H.-M., An, L.-K., Philpot, B.D., and Zylka, M.J. (2016).
893   Topoisomerase 1 Regulates Gene Expression in Neurons through Cleavage Complex-
894   Dependent and -Independent Mechanisms. PLoS One *11*, e0156439.

895   Matsumoto, K., Mitani, T.T., Horiguchi, S.A., Kaneshiro, J., Murakami, T.C., Mano, T.,
896   Fujishima, H., Konno, A., Watanabe, T.M., Hirai, H., et al. (2019). Advanced CUBIC tissue
897   clearing for whole-organ cell profiling. Nat. Protoc. *14*, 3506–3537.

898   McKinnon, P.J. (2016). Topoisomerases and the regulation of neural function. Nat. Rev.
899   Neurosci. *17*, 673–679.

900   Metz, C.T., Klein, S., Schaap, M., van Walsum, T., and Niessen, W.J. (2011). Nonrigid
901   registration of dynamic medical imaging data using nD + t B-splines and a groupwise
902   optimization approach. Med. Image Anal. *15*, 238–249.

903   Migliori, B., Datta, M.S., Dupre, C., Apak, M.C., Asano, S., Gao, R., Boyden, E.S., Hermanson,
904   O., Yuste, R., and Tomer, R. (2018). Light sheet theta microscopy for rapid high-resolution
905   imaging of large biological samples. BMC Biol. *16*, 57.

906   Milosevic, A., Liebmann, T., Knudsen, M., Schintu, N., Svenningsson, P., and Greengard, P.
907   (2017). Cell- and region-specific expression of depression-related protein p11 (S100a10) in the
908   brain. J. Comp. Neurol. *525*, 955–975.

909   Molyneaux, B.J., Arlotta, P., Menezes, J.R.L., and Macklis, J.D. (2007). Neuronal subtype
910   specification in the cerebral cortex. Nat. Rev. Neurosci. *8*, 427–437.

911   Murakami, T.C., Mano, T., Saikawa, S., Horiguchi, S.A., Shigeta, D., Baba, K., Sekiya, H.,
912   Shimizu, Y., Tanaka, K.F., Kiyonari, H., et al. (2018). A three-dimensional single-cell-resolution
913   whole-brain atlas using CUBIC-X expansion microscopy and tissue clearing. Nat. Neurosci. *21*,

914   625–637.

915   Murray, E., Cho, J.H., Goodwin, D., Ku, T., Swaney, J., Kim, S.-Y., Choi, H., Park, Y.-G., Park,
916   J.-Y., Hubbert, A., et al. (2015). Simple, Scalable Proteomic Imaging for High-Dimensional
917   Profiling of Intact Systems. Cell *163*, 1500–1514.

918   Pan, C., Cai, R., Quacquarelli, F.P., Ghasemigharagoz, A., Lourbopoulos, A., Matryba, P.,
919   Plesnila, N., Dichgans, M., Hellal, F., and Ertürk, A. (2016). Shrinkage-mediated imaging of
920   entire organs and organisms using uDISCO. Nat. Methods *13*, 859–867.

921   Park, Y.-G., Sohn, C.H., Chen, R., McCue, M., Yun, D.H., Drummond, G.T., Ku, T., Evans, N.B.,
922   Oak, H.C., Trieu, W., et al. (2018). Protection of tissue physicochemical properties using
923   polyfunctional crosslinkers. Nat. Biotechnol.

924   Pende, M., Becker, K., Wanis, M., Saghafi, S., Kaur, R., Hahn, C., Pende, N., Foroughipour, M.,
925   Hummel, T., and Dodt, H.-U. (2018). High-resolution ultramicroscopy of the developing and
926   adult nervous system in optically cleared Drosophila melanogaster. Nat. Commun. *9*, 4731.

927   Peng, T., Thorn, K., Schroeder, T., Wang, L., Theis, F.J., Marr, C., and Navab, N. (2017). A
928   BaSiC tool for background and shading correction of optical microscopy images. Nat. Commun.
929   *8*, 14836.

930   Renier, N., Adams, E.L., Kirst, C., Wu, Z., Azevedo, R., Kohl, J., Autry, A.E., Kadiri, L., Umadevi
931   Venkataraju, K., Zhou, Y., et al. (2016). Mapping of Brain Activity by Automated Volume
932   Analysis of Immediate Early Genes. Cell *165*, 1789–1802.

933   Richardson, D.S., and Lichtman, J.W. (2015). Clarifying Tissue Clearing. Cell *162*, 246–257.

934   Roskams, J., and Popović, Z. (2016). Power to the People: Addressing Big Data Challenges in
935   Neuroscience by Creating a New Cadre of Citizen Neuroscientists. Neuron *92*, 658–664.

936   Schubert, P.J., Dorkenwald, S., Januszewski, M., Jain, V., and Kornfeld, J. (2019). Learning
937   cellular morphology with neural networks. Nat. Commun. *10*, 2736.

938   Shamash, P., Carandini, M., Harris, K., and Steinmetz, N. (2018). A tool for analyzing electrode
939   tracks from slice histology.

940   Shattuck, D.W., and Leahy, R.M. (2002). BrainSuite: an automated cortical surface identification
941   tool. Med. Image Anal. *6*, 129–142.

942   Shin Yim, Y., Park, A., Berrios, J., Lafourcade, M., Pascual, L.M., Soares, N., Yeon Kim, J.,
943   Kim, S., Kim, H., Waisman, A., et al. (2017). Reversing behavioural abnormalities in mice
944   exposed to maternal inflammation. Nature *549*, 482–487.

945   Stoner, R., Chow, M.L., Boyle, M.P., Sunkin, S.M., Mouton, P.R., Roy, S., Wynshaw-Boris, A.,
946   Colamarino, S.A., Lein, E.S., and Courchesne, E. (2014). Patches of disorganization in the
947   neocortex of children with autism. N. Engl. J. Med. *370*, 1209–1219.

948   Stringer, C., Michaelos, M., and Pachitariu, M. (2020). Cellpose: a generalist algorithm for
949   cellular segmentation.

950   Sugino, K., Clark, E., Schulmann, A., Shima, Y., Wang, L., Hunt, D.L., Hooks, B.M., Tränkner,
951   D., Chandrashekar, J., Picard, S., et al. (2019). Mapping the transcriptional diversity of

952   genetically and anatomically defined cell populations in the mouse brain. Elife *8*.

953   Susaki, E.A., Tainaka, K., Perrin, D., Yukinaga, H., Kuno, A., and Ueda, H.R. (2015). Advanced
954   CUBIC protocols for whole-brain and whole-body clearing and imaging. Nat. Protoc. *10*, 1709–
955   1727.

956   Susaki, E.A., Shimizu, C., Kuno, A., Tainaka, K., Li, X., Nishi, K., Morishima, K., Ono, H., Ode,
957   K.L., Saeki, Y., et al. (2020). Versatile whole-organ/body staining and imaging based on
958   electrolyte-gel properties of biological tissues. Nat. Commun. *11*, 1982.

959   Tainaka, K., Kubota, S.I., Suyama, T.Q., Susaki, E.A., Perrin, D., Ukai-Tadenuma, M., Ukai, H.,
960   and Ueda, H.R. (2014). Whole-body imaging with single-cell resolution by tissue decolorization.
961   Cell *159*, 911–924.

962   Tasic, B., Yao, Z., Graybuck, L.T., Smith, K.A., Nguyen, T.N., Bertagnolli, D., Goldy, J., Garren,
963   E., Economo, M.N., Viswanathan, S., et al. (2018). Shared and distinct transcriptomic cell types
964   across neocortical areas. Nature *563*, 72–78.

965   Tomer, R., Ye, L., Hsueh, B., and Deisseroth, K. (2014). Advanced CLARITY for rapid and high-
966   resolution imaging of intact tissues. Nat. Protoc. *9*, 1682–1697.

967   Tsien, J.Z., Chen, D.F., Gerber, D., Tom, C., Mercer, E.H., Anderson, D.J., Mayford, M., Kandel,
968   E.R., and Tonegawa, S. (1996). Subregion- and cell type-restricted gene knockout in mouse
969   brain. Cell *87*, 1317–1326.

970   Ueda, H.R., Ertürk, A., Chung, K., Gradinaru, V., Chédotal, A., Tomancak, P., and Keller, P.J.
971   (2020). Tissue clearing and its applications in neuroscience. Nat. Rev. Neurosci. *21*, 61–79.

972   Voigt, F.F., Kirschenbaum, D., Platonova, E., Pagès, S., Campbell, R.A.A., Kastli, R., Schaettin,
973   M., Egolf, L., van der Bourg, A., Bethge, P., et al. (2019). The mesoSPIM initiative: open-source
974   light-sheet microscopes for imaging cleared tissue. Nat. Methods *16*, 1105–1108.

975   Voleti, V., Patel, K.B., Li, W., Perez Campos, C., Bharadwaj, S., Yu, H., Ford, C., Casper, M.J.,
976   Yan, R.W., Liang, W., et al. (2019). Real-time volumetric microscopy of in vivo dynamics and
977   large-scale samples with SCAPE 2.0. Nat. Methods *16*, 1054–1062.

978   Wang, Q., Ding, S.-L., Li, Y., Royall, J., Feng, D., Lesnar, P., Graddis, N., Naeemi, M., Facer,
979   B., Ho, A., et al. (2020). The Allen Mouse Brain Common Coordinate Framework: A 3D
980   Reference Atlas. Cell *181*, 936–953.e20.

981   Weigert, M., Schmidt, U., Boothe, T., Müller, A., Dibrov, A., Jain, A., Wilhelm, B., Schmidt, D.,
982   Broaddus, C., Culley, S., et al. (2018). Content-aware image restoration: pushing the limits of
983   fluorescence microscopy. Nat. Methods *15*, 1090–1097.

984   Ye, L., Allen, W.E., Thompson, K.R., Tian, Q., Hsueh, B., Ramakrishnan, C., Wang, A.-C.,
985   Jennings, J.H., Adhikari, A., Halpern, C.H., et al. (2016). Wiring and Molecular Features of
986   Prefrontal Ensembles Representing Distinct Experiences. Cell *165*, 1776–1788.

987   Yun, D.H., Park, Y.-G., Cho, J.H., Kamentsky, L., Evans, N.B., Albanese, A., Xie, K., Swaney,
988   J., Sohn, C.H., Tian, Y., et al. (2019). Ultrafast immunostaining of organ-scale tissues for
989   scalable proteomic phenotyping.

990   Zeisel, A., Muñoz-Manchado, A.B., Codeluppi, S., Lönnerberg, P., La Manno, G., Juréus, A.,

991   Marques, S., Munguba, H., He, L., Betsholtz, C., et al. (2015). Brain structure. Cell types in the
992   mouse cortex and hippocampus revealed by single-cell RNA-seq. Science *347*, 1138–1142.
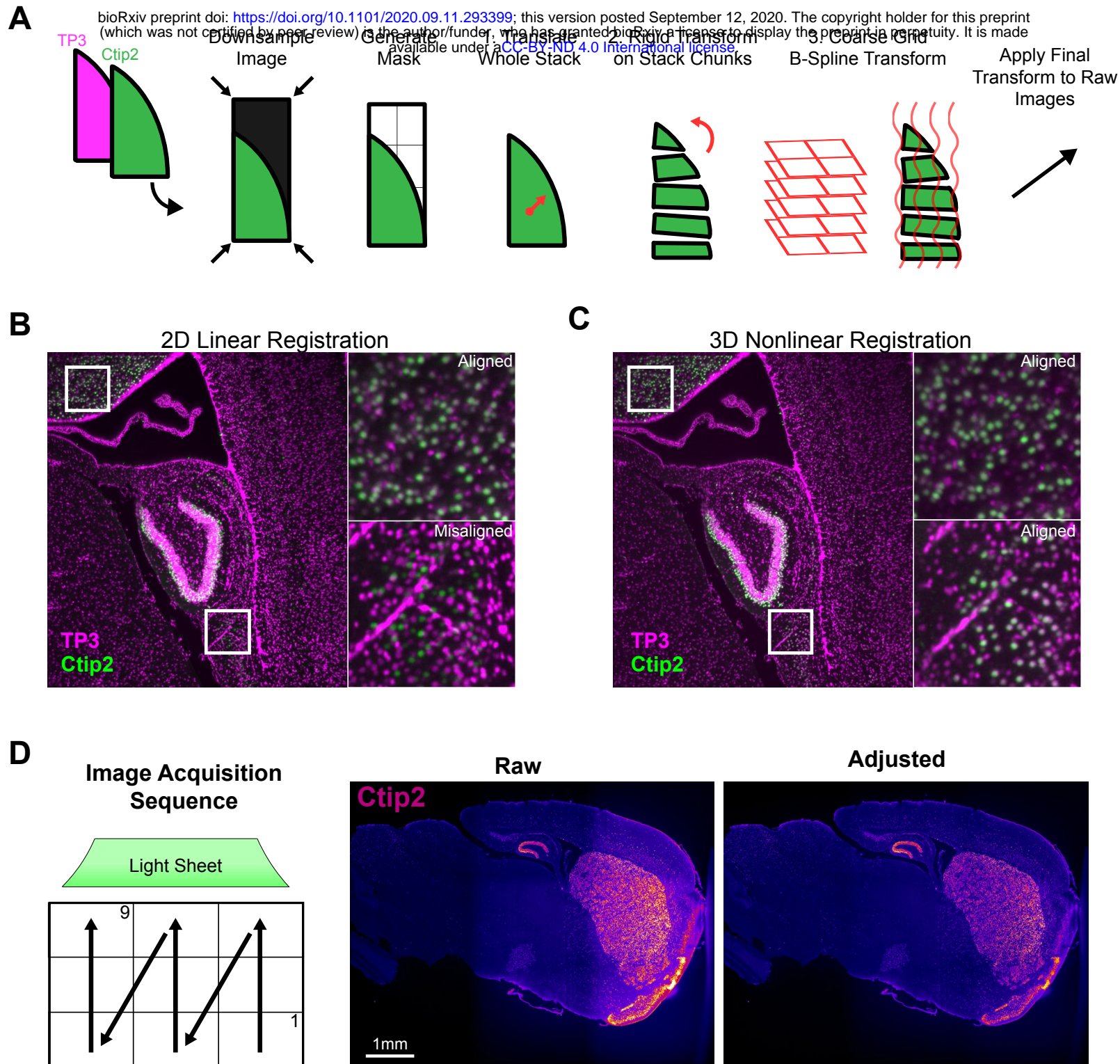
Figure S1, Related to Figure 1. Nonlinear Alignment and Intensity Adjustment of 3D Multichannel Images.

A. Overview of alignment procedures.

B. Example of channel misalignment after 2D registration by translation showing only part of the image aligning correctly.

C. Same section as in B after the nonlinear alignment procedure.

D. *Top1* cKO sample images of Ctip2 labeling with (right) or without (left) adjusting intensities for tile positions and light-sheet width.
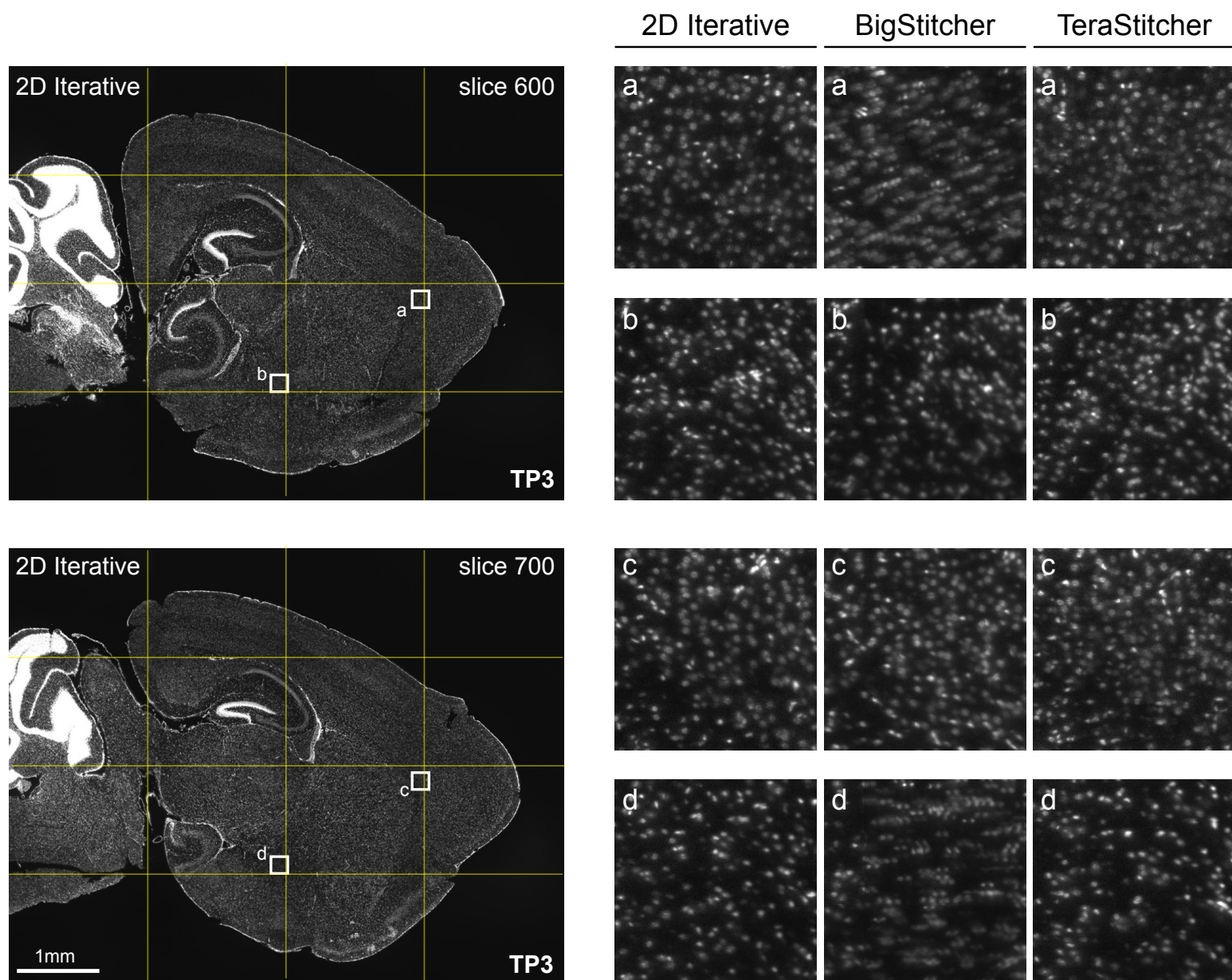
Figure S2, Related to Figure 1. Iterative 2D Stitching of Multi-Tile Light Sheet Images.
Sample results from 2D iterative stitching of WT mouse hemisphere compared with other dedicated 3D stitching software. Yellow lines indicate approximate stitching seams.

A
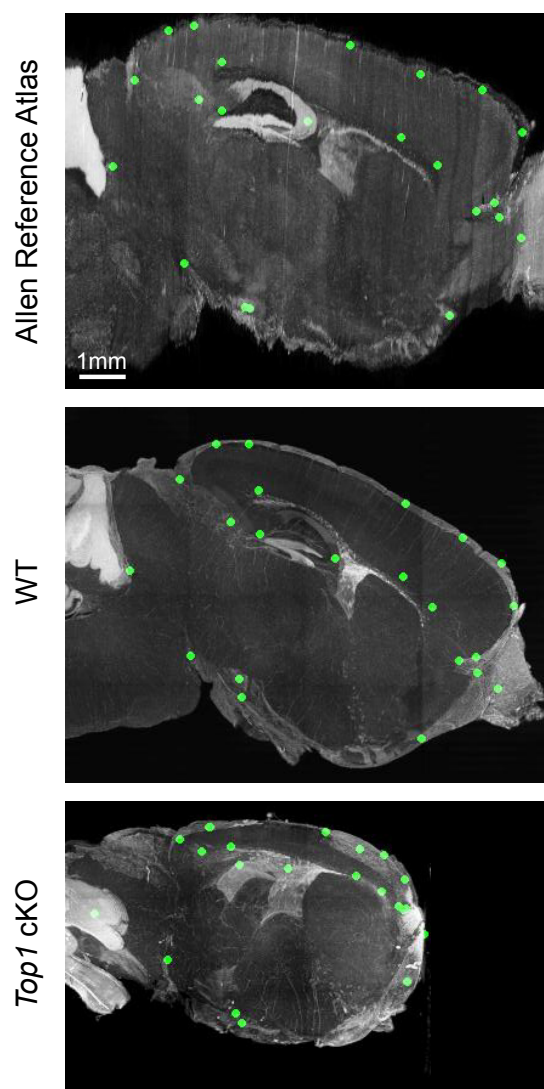
B
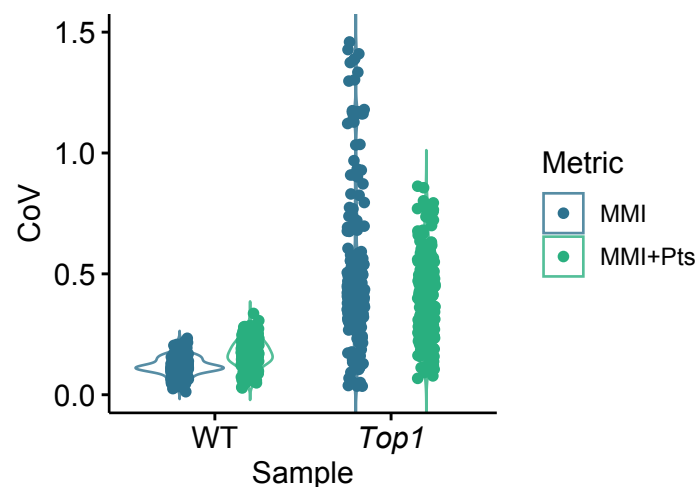
C

	WT (MMI)	WT (MMI+Pts)	*Top1* (MMI)	*Top1* (MMI+Pts)
DICE	0.917 (0.017)	0.923 (0.008)	0.526 (0.189)	**0.890 (0.013)**
CoV (All Cortical Structures)	0.124 (0.037)	0.167 (0.059)	0.524 (0.367)	0.422 (0.169)
CoV (Full Cortex Registered)	0.096	0.094	0.203	0.184
CoV (Full Cortex Manual)	0.081		0.242	

Figure S3, Related to Figure 2. Image Landmark Selection for Points-Guided Image Registration.

A. 1mm thick sagittal maximum intensity projection displaying corresponding points positions in ARA, WT, and Top1 cKO brain hemispheres.

B. Coefficients of variation (CoV) of structure volumes for all cortical annotations in the ARA after registration with or without corresponding points.

C. DICE scores and CoV metrics for indicated registration procedures. Data represented as mean (± standard deviation). CoV was calculated for individual ARA annotations (242 structures plotted in B) or the full isocortex after registration. These compared with the CoV for the full cortex based on manual annotation. Bold value: Top1 MMI/Top1 MMI+ Pts, p < 0.001.
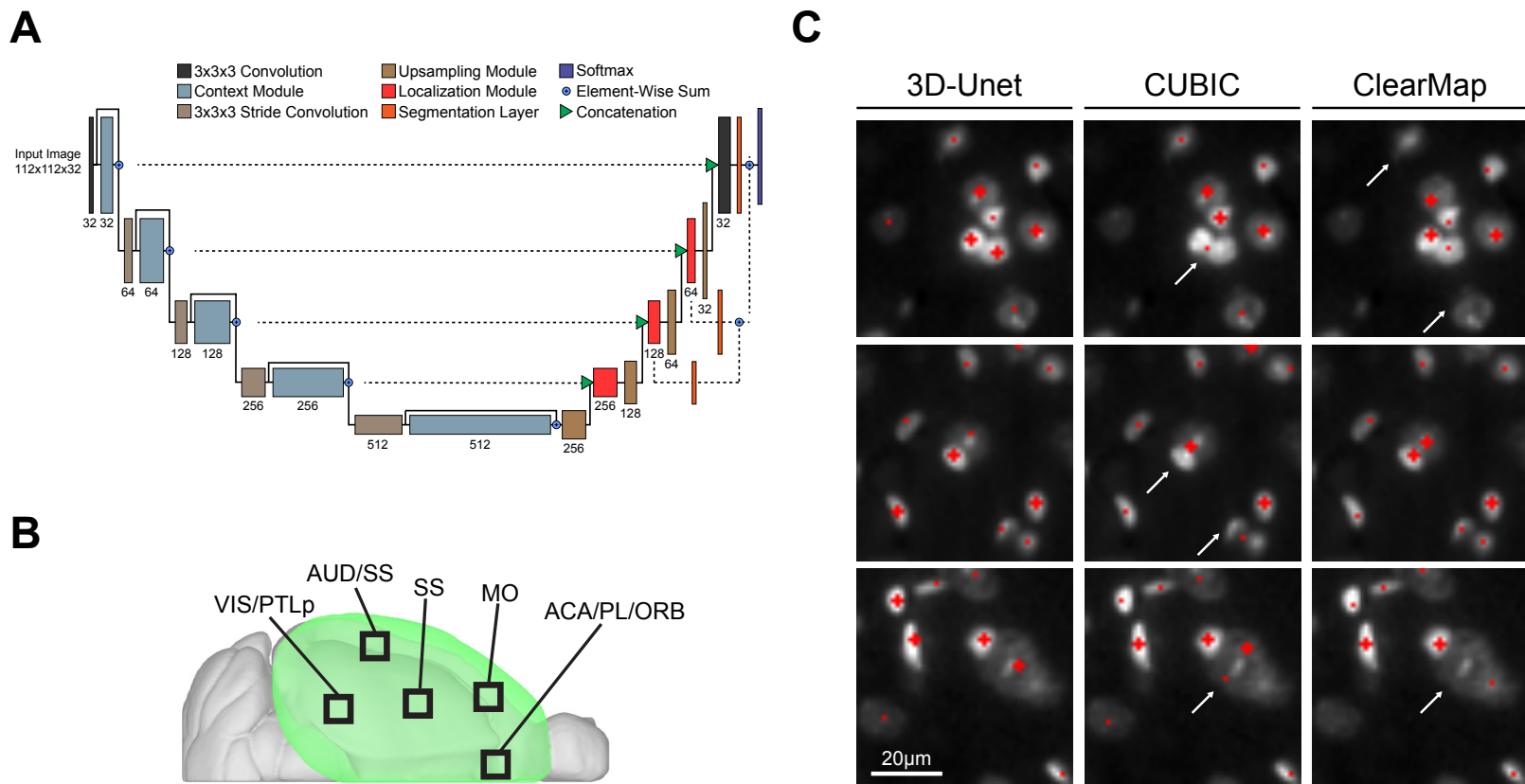
A

B

C

Figure S4, Related to Figure 3. 3D-Unet Training and Evaluation.

A. 3D-Unet architecture adapted from Isensee et al. 2018.

B. Approximate patch locations used for training the 3D-Unet nuclei detection model

C. Example images of nuclei detection results. Cross symbols indicate centroids in the displayed z slice whereas points indicate centroids in slices directly above or below. Arrows indicate detection errors in the full 3D volume.
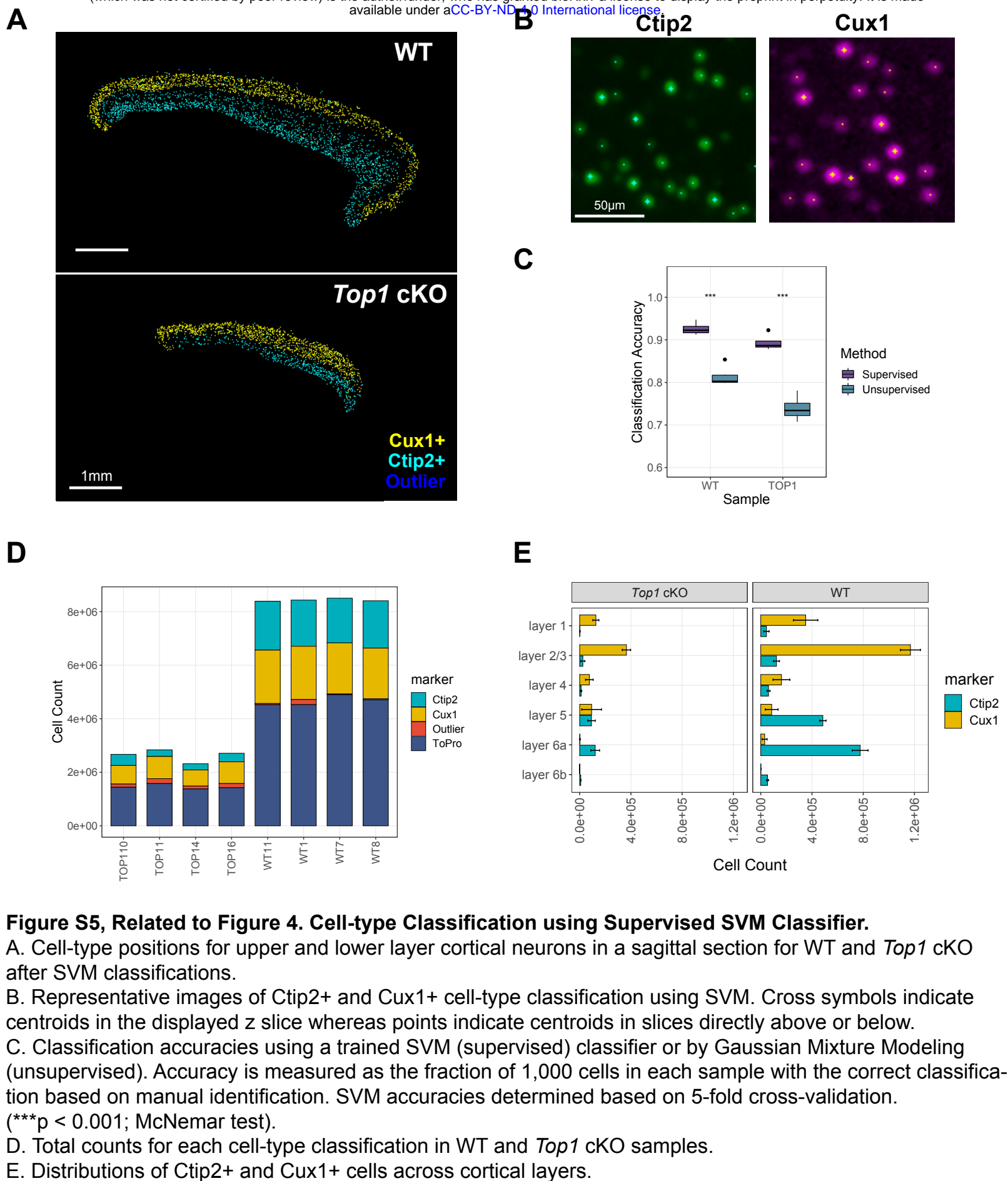
Figure S5, Related to Figure 4. Cell-type Classification using Supervised SVM Classifier.
A. Cell-type positions for upper and lower layer cortical neurons in a sagittal section for WT and *Top1* cKO after SVM classifications.
B. Representative images of Ctip2+ and Cux1+ cell-type classification using SVM. Cross symbols indicate centroids in the displayed z slice whereas points indicate centroids in slices directly above or below.
C. Classification accuracies using a trained SVM (supervised) classifier or by Gaussian Mixture Modeling (unsupervised). Accuracy is measured as the fraction of 1,000 cells in each sample with the correct classification based on manual identification. SVM accuracies determined based on 5-fold cross-validation. (***p < 0.001; McNemar test).
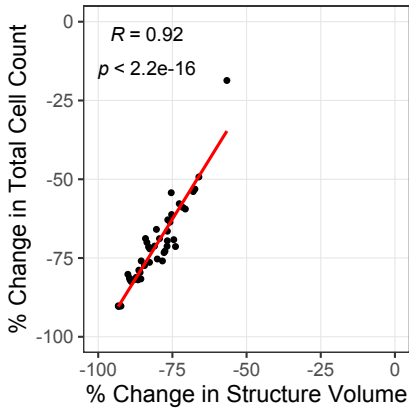D. Total counts for each cell-type classification in WT and *Top1* cKO samples.
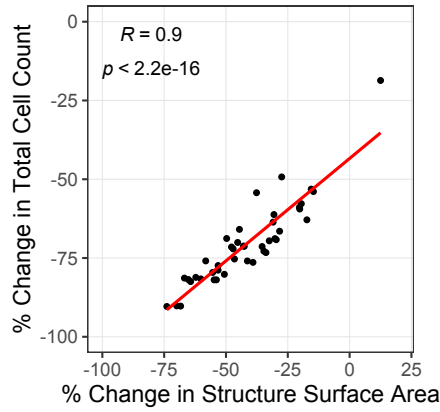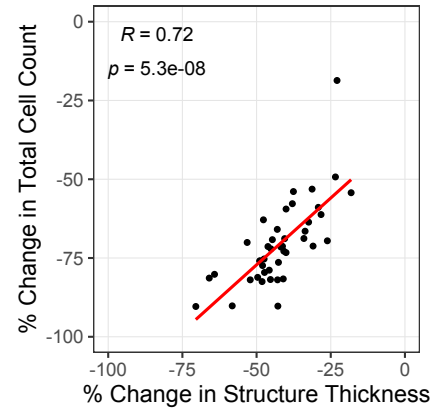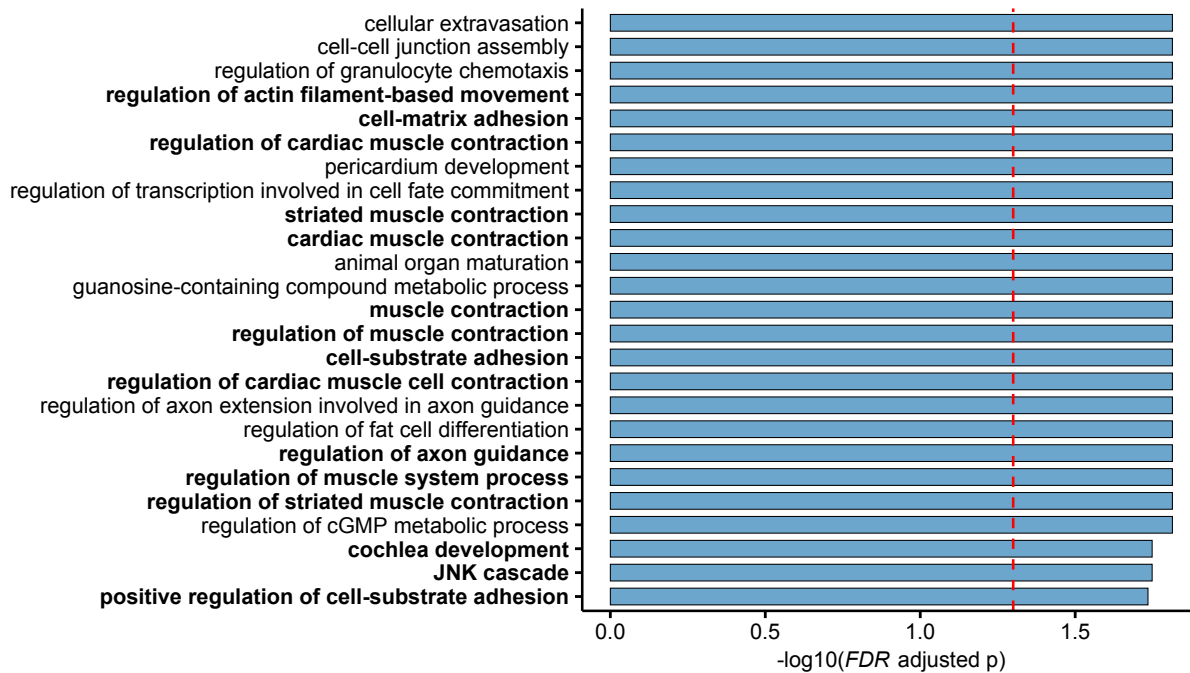E. Distributions of Ctip2+ and Cux1+ cells across cortical layers.
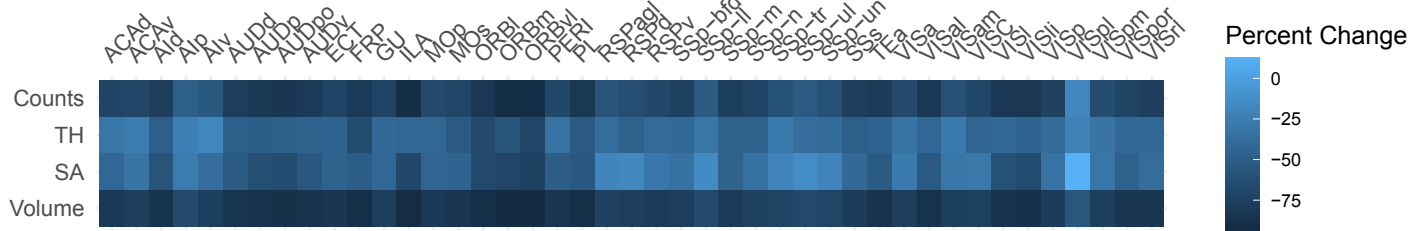
Figure S6, Related to Figure 6. Structural and Molecular Associations with Cell Loss in the *Top1* cKO Model.

A. Heatmap displaying percent change in cortical cell count, volume, surface area, and thickness for each cortical region.

B-D. Correlation between total cell count difference and volume (B), surface area (C), and thickness (D) across cortical regions.

E. Gene ontology showing the top 25 most significant categories correlated with neuron loss in *Top1* cKO. Bolded categories contain at least 1 gene differentially expressed in *Top1* cKO from scRNA-seq studies.

Table S1, Related to Figure 4. Volume, Cell Count, and Cell Density Statistics for *Top1* cKO.
Cell counts and densities are summed for all counted nuclei after removing outliers (ToPro) as well as cells classified Ctip2+ or Cux1+.

Video S1, Related to Figure 4. Visual Comparison of WT and *Top1* cKO Brain Hemispheres.
Representative examples of iDISCO-processed WT and Top1 cKO samples labelling TO-PRO-3 (white), Ctip2 (green), and Cux1(magenta). Images were downsampled to 10 µm/voxel for smoother rendering. Cortical cell-type classifications displayed as point clouds (white: Ctip2-/Cux1-, teal: Ctip2+, yellow: Cux1+).

Video S2, Related to Figure 4. 3D Inspection of NuMorph Nuclei Counting and Cell-type Classification.
Visualization of a 400 µm thick WT sagittal section at 1.21x1.21x4 µm/voxel resolution labelling TO-PRO-3 (white), Ctip2 (green), and Cux1(magenta). Cortical cell-type classifications displayed as point clouds (white: Ctip2-/Cux1-, teal: Ctip2+, yellow: Cux1+).